Combustion and Flame xxx (xxxx) xxx

Contents lists available at ScienceDirect

Combustion and Flame

journal homepage: www.elsevier.com/locate/combustflame

A comprehensive modeling procedure for estimating statistical properties of forced ignition

Q1 Yihao Tang[a,*], Malik Hassanaly[a], Venkat Raman[a], Brandon Sforzo[b], Jerry Seitzman[c]

[a] Department of Aerospace Engineering, University of Michigan, Ann Arbor, MI 48109, USA
[b] Energy Systems Division, Argonne National Laboratory, Argonne, IL 60439, USA
[c] School of Aerospace Engineering, Georgia Institute of Technology, Atlanta, GA 30332, USA

ARTICLE INFO

Article history:
Received 19 December 2018
Revised 8 February 2019
Accepted 23 April 2019
Available online xxx

Keywords:
Forced ignition
Relight
Uncertainty quantification
Turbulence
Large eddy simulation

ABSTRACT

A comprehensive modeling procedure for estimating the probability of ignition with application to high altitude relights of aircraft combustors is developed. In these configurations, an ignitor is used to introduce high-enthalpy discharge into a fuel-laden but stratified flow. Due to the inherent variabilities inflow conditions, kernel discharge process, and the chaotic turbulent flow, ignition cannot be described deterministically, but only as a probabilistic measure. The proposed modeling framework consists of three components. The turbulent flow is represented using the large eddy simulation (LES) framework. The ignition process is modeled using a manifold approach, where the initial kernel evolution is represented using a homogeneous reactor while the latter part of the evolution is represented as a competition between diffusion and chemical reactions using a flamelet-type mapping. A combined lookup table that can track the evolution of the kernel through these two distinct reaction stages is developed. The table lookup variables are solved within the LES framework. The resulting simulation tool is then embedded within an uncertainty quantification approach, where variations in the turbulent flow, as well as operating and kernel properties, are simulated using a Monte-Carlo-based sampling approach. Techniques to reduce computational cost are used to obtain a robust, numerically accurate, and physically representative model for engine relight. The method is validated using experimental data for ignition of methane/air mixtures. Due to the comprehensive nature of the modeling procedure, it is found that the simulation tool reproduces experimentally observed ignition probabilities over a wide range of operating conditions.

1. Introduction

The ability to re-ignite or relight an aircraft engine at high altitude is not only a safety constraint but a certification requirement as well. Due to the highly chaotic and unsteady flow conditions inside the combustor, ensuring a fast and robust relight process is a design challenge. Conceptually, the re-ignition process consists of fueling the combustor adequately, followed by the introduction of a spark that supports the growth of a flame kernel that eventually stabilizes in the combustor. Since a spark is used to reignite the combustor, this process is termed forced ignition. The spark introduces a pocket of hot fluid as well as ionized or free radical species into the flow. In order to sustain and develop into a stable flame, the hot kernel needs to survive thermal diffusion as well as turbulent mixing. If a large enough part of the kernel reaches a sufficiently low-velocity region within the flammable limits, it can then stabilize to form a fully-developed flame front. Otherwise, the flame does not sustain and the ignition failed. The stabilization of the flame depends on a large number of variables affecting the ignition process. In particular, the strength of the re-ignition spark as well as the properties of the fuel play an important role [1,2]. As a result, substantial effort has been devoted to the design of jet fuel [2–4] to facilitate the ignition process. In practice, different fuels are experimentally tested to evaluate their ignition characteristics at different operating conditions. However, even in well-characterized experiments, it is difficult to replicate and control all the physical parameters that affect the ignition process. Hence, detailed computational models are necessary to provide both qualitative and quantitative insight into the complex relight process. In particular, the focus of this work is on the development of models that can predict the probability of ignition at particular operating conditions.

To model the forced ignition process, the evolution of the spark kernel into a spatially distributed flame front needs to be de-

* Corresponding author.
E-mail address: yhtang@umich.edu (Y. Tang).

https://doi.org/10.1016/j.combustflame.2019.04.045
0010-2180/

Nomenclature

$\dot{\omega}_\Psi$	reaction source of variable Ψ
$\mathcal{R}_{PCE}$	residual of the truncated polynomial chaos expansion
$\|\nabla\rho\|_{Norm}$	density gradient magnitude normalized to [0,1]
μ_Ψ	mean value of variable Ψ
ϕ	global equivalence ratio
ρ_0	pre-discharge density
σ_Ψ	standard deviation of variable Ψ
τ_{ker}	duration time of kernel enthalpy boundary enforcement
ε_{Spl}	statistical sampling error
Ξ	ensemble of N initial turbulent flow fields
ξ	initial turbulent flow field
C	progress variable: $Y_{CO_2}+Y_{CO}$
C_i	the ith point of the tabulation C-axis
C_{target}	target value of progress variable applied to reconstruct $S_{C,r}$
E_d	spark deposit energy: thermal energy received by the gas phase from a spark discharge
E_n	spark nominal energy: electric energy input of a spark discharge
h	total enthalpy
h_0	pre-discharge total enthalpy
h_c	total enthalpy at the center point of the kernel inject boundary
h_{ker}	characteristic value of kernel total enthalpy
I	ignition indicator of success and failure
K	kernel parameters that describe the initial kernel
N	number of samples applied to compute empirical mean
O	operating conditions
$P_{Igni\|E_d,PCE}$	response surface of $P_{Igni\|K,Spl}$ obtained with polynomial chaos expansion
$P_{Igni\|E_d,Spl}$	estimator of $P_{Igni\|E_d}$ with statistical sampling
$P_{Igni\|E_d}$	ignition probability conditioned on E_d
$P_{Igni\|K,Spl}$	estimator of $P_{Igni\|K}$ with statistical sampling
$P_{Igni\|K}$	ignition probability conditioned on K
P_{Igni}	exact probability of ignition
q	truncation order of polynomial chaos expansion
r	radial distance to the center of kernel inject boundary
$r_{ignitor}$	radius of the ignitor top surface
$S_{C,r}$	integrated progress variable source in novel reconstruction method
$S_{C,t}$	integrated progress variable source in conventional tabulation
S_C	exact integrated progress variable source
T	preheat temperature of main flow
t_{init}	initiation time of kernel enthalpy and velocity boundary enforcement
t_{term}	termination time of kernel velocity boundary enforcement
U_c	velocity magnitude at the center point of the kernel inject boundary
U_{ker}	characteristic velocity of the injected kernel
U_{main}	main flow bulk velocity
V_{cav}	volume of the ignitor cavity
V_{ker}	volume of the injected kernel
Y_i	mass fraction of species i
Z	mixture fraction
$\Delta t_{HR,Tab}$	time interval between two consecutive tabulation points of HR time history
Δt_{Sim}	simulation time step
Δt_{Tab}	tabulated time information applied to reconstruct $S_{C,r}$

scribed. Such ignition processes are found in internal combustion engines, where prior studies have focused on model development [5–9]. For instance, Lagrangian particles have been used to track early kernel development [5–8], which then transitions to a sustained flame front. This final flame process is modeled using conventional combustion models such as a time scale model [5], flame surface density (FSD) model [7,8], or level set/G-equation combustion model [6]. The transition between the ignition model and the conventional combustion model is imposed using switching functions.

Unlike in IC engines, forced ignition in aircraft engines is not only affected by strain rate variations but also by equivalence ratio fluctuations, where non-uniform fuel distribution can lead to strong non-local effects. For instance, in a non-premixed configuration, a spark placed in a region with equivalence ratio outside the flammability limit can lead to a successful ignition through kernel transport and mixing [10]. In this regard, previous studies have combined special field initialization treatments (to model the ignition) with transport-based combustion models (to model the spark kernel and the flame propagation) at conditions typical of aircraft combustors. Triantafyllidis et al. [11] used a conditional moment closure (CMC) approach to study the ignition of a bluff-body stabilized flame, with the spark initialized as a pocket of burnt product. Results showed that convection and diffusion of hot products from the recirculation zone to the unburnt mixture promoted flame stabilization. Subramanian et al. [12] and Pillai [13] have applied energy deposition (ED) to represent the ignition kernel, where ED is followed by a continuous monitoring of the local gas phase temperature. The chemical reaction is triggered when the local post-deposition temperature drops to the level of chemical equilibrium and is initiated by patching the scalar field of products at equilibrium conditions. The non-premixed ignition process may be split into three phases [14]: phase 1, generation of small flame around the spark; phase 2, the transition from flame kernel into propagating flame; phase 3, long-term flame stabilization within the burner. An additional phase can be defined for a realistic engine as phase 4, flame propagation among multiple combustors [15]. A clear definition of the applicability by these four phases is critical for evaluating an ignition model. When the ignition procedure consists of altering the flow field, the method implicitly assumes the successful development of the kernel, and such methods are useful for studying phases 3 and 4 [11,15]. In altitude relight problems, the success/failure of ignition is dependent on the outcome of phases 1 and 2. Apart from applying field initialization to existing combustion models, directly solving for the finite-rate chemistry and applying ED to the energy equation is another common approach to simulate forced ignitions. This method does allow variable outcomes for phases 1 and 2 but also involves high computational cost. Previous studies are mostly limited to mechanisms using global reactions [16–18], where the reaction model should be capable of capturing the ignition process adequately. For realistic combustion systems that use jet fuels, this method may become inaccurate due to the complex heat release process.

Since the ignition outcome (success or failure) is not only influenced by deterministic parameters (ambient temperature, pressure, global equivalence ratio) but also aleatoric parameters (variable strain rate next to the spark, fuel mixing, spark properties), it is meaningful to compute a probability of ignition for each deterministic operating condition. In general, estimating probabilities of events from computations is a computational challenge

Please cite this article as: Y. Tang, M. Hassanaly and V. Raman et al., A comprehensive modeling procedure for estimating statistical properties of forced ignition, Combustion and Flame, https://doi.org/10.1016/j.combustflame.2019.04.045

in itself, due to the increased cost of propagating uncertainties [19,20]. This is true in particular for problems that are not statistically stationary such as the one investigated here [21]. However, several experimental studies are available in the literature. Birch et al. [22] measured the ignition probability of a turbulent non-premixed jet flame with spark discharge and found that the probability of obtaining a flame kernel at some spatial location can be approximated by the local probability of having a mixture fraction within the flammability limits. Ahmed and Mastorakos [23] carried out a similar experiment to measure the ignition probability as a function of mixture fraction, and found that final successful or failed ignition does not always take place in or out of the flammability limits, respectively, due to transport effects. Cordier et al. [24] measured the ignition probability in a swirl combustor. Although the system is nominally premixed, the ignition efficiency was controlled not only by the local flow properties but the kernel trajectory. Recently, Sforzo [25] designed a facility that closely replicates the ignition process of aircraft engines and where it is possible to measure the ignition probability of different jet fuels. In this particular combustor, the spark discharge is initialized within a non-reactive flow before the hot kernel later mixes with flammable fluid. Here, this configuration is simulated in order to illustrate the capabilities of the model developed. Further details will be presented later. Numerical studies that measure the probability of ignition are mostly based on cold flow simulations or reduced order modeling since the measurement often requires simulating a large number of flow realizations. For example, Lacaze et al. [16] estimated the ignition probability based on the local probability distribution of mixture fraction and flow velocity provided by cold flow LES. A similar method has been applied to study ignition of two-phase flow by Eyssartier et al. [26]. In the study of Neophytou et al. [27] the kernel trajectory is tracked using Lagrangian particles. The particles move according to a stochastic model. As the particles move, they can ignite parts of the domain that were initially cold. The simulation is repeated multiple times to obtain the ignition probability. Similar strategies based on kernel trace tracking have also been developed elsewhere [28,29]. Based on the two strategies of using local flow properties and kernel traces, Esclapez further developed a blended model where the ignitability of a kernel can evolve based on the local turbulence properties encountered along its trajectory [30]. In these methods, in order to make the ignition probability computation tractable, strong assumptions about the interaction between the kernel and the non-reacting flow field are made. In the study of [31], Sforzo and Seitzman simplified the ignition kernel to a well-stirred reactor with a staged constant inflow to account for entrainment. This work used detailed methane chemistry a reduced-order model developed and inputs based on experimental measurements to initialize the numerical computations. The model supplied ignition results across the input design space, which was the basis for a support vector machine classification algorithm. By sampling input variables using experimentally calibrated distributions, the tool provided ignition probabilities that could be compared to experimental measurements. Though computationally efficient, this methodology treats the turbulent mixing and diffusion processes that dictate the stochastic nature of ignition as direct inputs, which do not allow for spatial and temporal variations in a given simulation. In terms of hot flow simulations, Esclapez et al. [18] have simulated ignition of a partially premixed combustor using LES and two-step chemistry with ED. Despite being one of the few studies that managed to estimate ignition probability based on hot flow simulations, the study has two major limitations: the kernel energy is tested at a fixed level, which does not include stochasticity of the spark discharge; ignition probability is sampled at a few independent locations without quantifying the uncertainties, making it difficult to evaluate the accuracy of the modeling strategy.

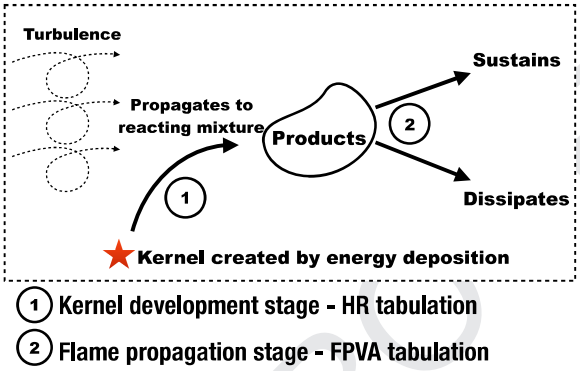

Fig. 1. Schematic of forced ignition in an aircraft engine and the proposed model decomposition.

With this background, the focus of the current study is (1) to develop a combustion model able to replicate the ignition outcomes of realistic jet fuels in a turbulent flow and (2) apply this model to estimate the probability of ignition at various operating conditions. For this purpose, additional issues due to chemistry have to be handled. In particular, the ignition temperature for the kernels is in the range where low-temperature chemistry for higher hydrocarbons is active. Therefore, detailed chemical kinetics effects need to be included in the model. At the same time, since multiple flow realizations need to be run, the individual simulation cost should be kept as low as possible. A tabulated chemistry approach that takes into account detailed kinetics, and handles both kernel development and the flame transition is developed. In Section 2, this tabulation-based ignition model is described. This model is then tested using the experimental configuration at the stratified flow facility at Georgia Institute of Technology [25,32]. The flow configuration along with the numerical algorithm used are explained in Section 3. In Section 4, a series of ignition cases in the aforementioned geometry are presented, followed by an analysis of the ignition behavior and mechanism. Further, in Section 5, an ensemble of LES calculations is performed to estimate the probability of ignition under various operating conditions of global temperatures and equivalence ratios. A non-intrusive uncertainty quantification approach is used to provide a direct comparison with the experimental data available.

2. Detailed modeling of ignition process

The purpose of this work is to develop a detailed ignition model that can be used in high-fidelity computational fluid dynamics approaches. Since ignition can only be described probabilistically, the development of a detailed model needs to take into account the unique nature of ignition physics in turbulent flow environments. In order to ensure predictive accuracy, the model consists of three components: (a) a physical representation of the ignition process that allows for flame development from a hot ignition kernel to be captured, (b) the coupling between the ignition kernel and the turbulent flow, and (c) the inclusion of inherent uncertainties in the ignition process in evaluating the outcome of a kernel injection.

The aircraft engine relight is here viewed as a process that goes through two main stages, each one corresponding to a different physical process. A schematic of the ignition process along with the corresponding modeling strategy is summarized in Fig. 1. Here, the term “spark” refers to the electric arc created during the ignitor discharge, whereas the term “kernel” refers to the high energy fluid pocket created by the energy deposition method. The model describes the initial kernel mixing and ignition as a homogeneous reaction process where chemical reactions alone govern the thermodynamic state (stage 1), while the flame develop-

Please cite this article as: Y. Tang, M. Hassanaly and V. Raman et al., A comprehensive modeling procedure for estimating statistical properties of forced ignition, Combustion and Flame, https://doi.org/10.1016/j.combustflame.2019.04.045

ment and stabilization as a diffusion-controlled process where flow and chemical timescales interact (stage 2). This two-stage definition is a physics-based simplification of the 4 ignition phases summarized in the last section. Specifically, phase 1 is governed by quasi-homogeneous reaction (stage 1), phases 3 and 4 are governed by diffusion-reaction balance (stage 2), whereas phase 2 is in the intermediate reaction mode between stage 1 and 2. The model developed here uses a tabulated chemistry approach. The table is constructed by blending solutions from different canonical combustion configurations that best represent each one of the two stages. As a result, the lookup table contains two types of canonical solutions: (a) a constant pressure homogeneous reaction (HR) for the kernel ignition stage; (b) a flamelet progress variable approach (FPVA) for the flame propagation stage. An additional type (c) is defined as the blend between (a) and (b). The modeling strategy hence has included all 4 phases of the forced ignition process.

Since total enthalpy of a representative kernel monotonically decreases due to turbulent mixing and diffusion, it is a good marker for tracking the ignition process. As the flow evolves, the switch from HR to FPVA must occur when the total enthalpy drops below a certain threshold. Therefore, the chemistry is tabulated as a function of total enthalpy h. In order to track the fuel–air mixing and the advancement of the reaction in the HR and FPVA model, the chemistry is also tabulated with respect to mixture fraction Z and progress variable C. Here, C is defined as the linear combination of species mass fraction, $C = Y_{CO} + Y_{CO_2}$, similar to definitions used elsewhere [33,34]. It is shown later that this definition captures the ignition process accurately as compared to direction numerical simulations.

These two tabulation strategies (HR and FPVA) cover different regions of the table phase space. HR is used for the high enthalpy space and FPVA for the low enthalpy space, and are simply combined into a unified table with the overlap region tabulated as a linear combination of the two individual maps. When the tabulation is implemented in simulations, a kernel is initialized as a pocket of high enthalpy, which falls into the region of HR tabulation. If the local flow properties described by $\{Z, h\}$ are favorable to ignition, the high chemical source from HR tabulation allows C to increase and initiate the reaction. As the flow field evolves and the spark energy dissipates out, the total enthalpy drops and automatically falls into the phase space of FPVA tabulation. Hence the following flame propagation or dissipation seamlessly transitions as the simulation proceeds in time. The HR and FPVA tabulation strategies are explained in depth in the next two subsections.

Before detailing the tabulation techniques, the choice of the chemical mechanism used is briefly explained. The chemical mechanism was selected based on its ability to reproduce the ignition delay time. Since the study focuses on methane/air combustion, the GRI3.0 [35] was found to be the best choice. This mechanism is used in the following sections for the HR and FPVA tabulation. Note that the model presented here can be adapted to other fuels by simply choosing a different chemical mechanism at this stage. For example, realistic jet fuels were simulated in Ref. [36,37]. Crucially, because a tabulated chemistry technique is used, the nature of the fuel does not affect the computational cost of the CFD simulation.

2.1. HR tabulation

The HR tabulation is inspired by the study of Pera et al. [38], which uses an HR model to simulate diesel engine ignition. There, the auto-ignition process is driven by compression-based pressure gain, and the forced ignition is treated locally as a homogeneous reaction caused by enthalpy rise. The fundamental idea here is to assume the local reaction time scale in a forced ignition event is much smaller than the transport time scales, so that the ignition core can be treated as reaction-dominant. Stratification effects are then included in the tabulation by combining different HR solutions for a range of equivalence ratios and unburnt temperatures. Specifically, each HR solution provides information of reaction process versus time which can be mapped on the C space at a constant $\{Z, h\}$; a series of HR solutions at different Z values provides information of stratification effects on reaction, and HR solutions with different unburnt temperatures allow a mapping in total enthalpy space h. The entire set of HR solution can be tabulated as a function of $\{C, Z, h\}$.

The HR calculations are performed using CANTERA [39], an open source solver. Time history of species was stored for each HR calculation. In order to keep a smooth ignition trajectory in time and progress variable phase space, the HR solutions are stored whenever one of the following three criteria is met: (a) the temperature increment exceeds 5 K since last output; (b) the progress variable percentage increment exceeds 5% since last output; (c) the time increment exceeds 1 s since last output. The HR calculation is terminated after it can be safely considered that the time exceeds the largest possible flow time scale, here considered to be below 7.5 s. A total number of 3330 HR calculations were performed for 90 levels of initial temperatures in the range {875 K, 3100 K}, and 37 levels of equivalence ratios spanning {0.3, 6.5} clustered near stoichiometric condition. These boundaries of operating conditions are enforced due to the following two reasons: (a) outside the lower temperature limit, or the fuel lean/rich limit, ignition delay will be longer than the largest flow time scales; (b) outside the upper temperature limit, the burnt temperature will breach the upper bound of the thermodynamic model (3500 K).

While the HR solutions contain all the necessary information of the ignition history profiles, the tabulation of these values for use in the CFD solution can lead to some numerical issues. In the CFD approach, a transport equation is solved for the three variables used to map the solution space (h, Z and C). Of these, the progress variable equation contains a chemical source term, which is obtained from the table. The exact integrated progress variable source term over a timestep is defined as

$$S_C = \frac{1}{\Delta t_{Sim}} \int_{t=0}^{t=\Delta t_{Sim}} \dot{\omega}_C(t) dt, \tag{1}$$

where $\dot{\omega}_C$ is the instantaneous progress variable source term, and Δt_{Sim} is the simulation timestep. In conventional tabulations, the integrated source term $S_{C,t}$ is often obtained by assuming a constant progress variable source term over a timestep [40] with an expression of the type:

$$S_{C,t} = \overline{\dot{\omega}_C(t = \Delta t_{Sim}/2)}, \tag{2}$$

where, $\overline{\dot{\omega}_C}$ is the progress variable source term that is interpolated from the discrete tabulation points on the table. This is based on the mid-point rule for integration and is accurate as long as the time-step is not large. However, for the purpose here, this approach may be erroneous. In the above formulation, two levels of approximation are made: (a) the reaction source term is assumed constant over the timestep and (b) the reaction source term is interpolated to $C(t = \Delta t_{Sim}/2)$ since it is only tabulated at discrete values of C. Since the ignition delay is of primary importance here, it is, therefore, crucial to correctly capture the early stages of the HR calculation (say between $C = 0$ and $C = 0.1$). There, the chemical source term is low enough such that approximating the source term constant over the simulation timestep (dictated by the flow) is reasonable. However, the source term interpolation can introduce an error that is large compared to the instantaneous value of the progress variable. Moreover, because the progress variable source term follows a convex profile with respect to progress variable at the early stages of ignition, the interpolation error always overestimates the integrated source term S_C. This is illustrated in

Please cite this article as: Y. Tang, M. Hassanaly and V. Raman et al., A comprehensive modeling procedure for estimating statistical properties of forced ignition, Combustion and Flame, https://doi.org/10.1016/j.combustflame.2019.04.045

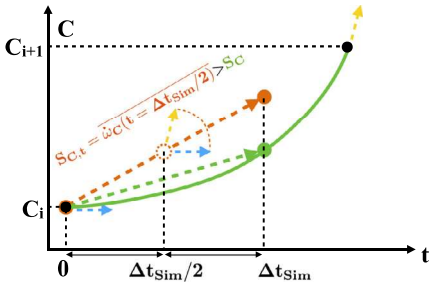

Fig. 2. Demonstration of interpolation error in conventional tabulation strategy at early stage of ignition. The time history profile (green solid line) and the tabulation C-axis (black dots) are created artificially for demonstration purposes. The integrated reaction source $S_{C,t}$ is indicated by the slope of the red dashed line. (For interpretation of the references to color in this figure legend, the reader is referred to the web version of this article.)

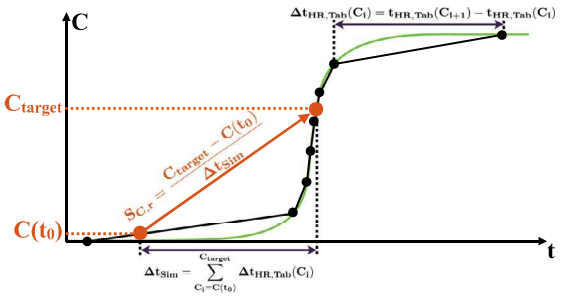

Fig. 3. Tabulation and lookup strategy of $S_{C,r}$. The time history profile and the tabulation C-axis are created artificially for demonstration purposes. (For interpretation of the references to color in this figure, the reader is referred to the web version of this article.)

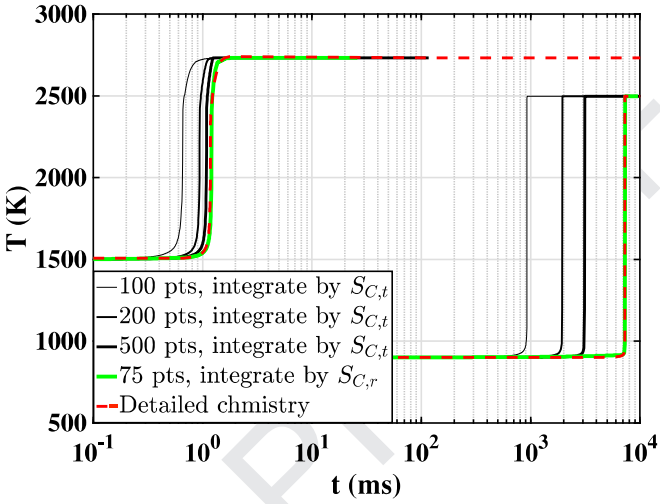

Fig. 4. Ignition time history obtained from time integration of directly tabulated reaction source with different resolutions of C-axis (black), the new tabulation/table lookup strategy (green), and detailed chemistry calculation of homogeneous reaction (dashed red). The operating conditions are set to 1 atm and stoichiometry. (For interpretation of the references to color in this figure legend, the reader is referred to the web version of this article.)

Fig. 2, where it can be seen the simulation time step Δt_{Sim} is small compared to the interval between two HR tabulation points (black dots), and the overestimation of interpolated reaction source (red dash arrow) is contributed from the higher reaction source at the next tabulation point (yellow dash arrow). This issue can be resolved by sufficiently refining the table, but this could become quickly intractable in terms of memory requirements.

A different tabulation/table lookup strategy is developed to resolve this issue. Here, $\dot{\omega}_C$ is no longer directly tabulated to avoid the corresponding interpolation error. The *time information* of the HR solution is tabulated instead, and $\dot{\omega}_C$ is reconstructed on-the-fly using this tabulated time information. The goal here is to obtain from the tabulation, the progress variable source term integrated over the simulation timestep instead of the instantaneous progress variable source term. The reconstructed reaction source S_C, r is written as

$$S_{C,r}(C(t_0), \Delta t_{Sim}) = \frac{C_{target} - C(t_0)}{\Delta t_{Sim}}, \tag{3}$$

where $S_{C,r}$ depends on the initial progress variable $C(t_0)$, the current simulation step size Δt_{Sim} and C_{target}, which is the theoretical final value of progress variable using the HR model combustion model. As $C(t_0)$ and Δt_{Sim} are already available at the current time step, the goal is to find $C_{target} = C_{HR}(t_0 + \Delta t_{Sim})$. The function C_{HR} takes time as an argument and is the time history profile of the progress variable along the HR profile.

The numerical procedure to obtain C_{target} is illustrated in Fig. 3 and explained below: the time history of the original HR solution is referred to as $t_{HR} = t_{HR}(C)$, or conversely $C_{HR} = C_{HR}(t)$. All tabulated properties are labeled by subscript "*Tab*", and their value at the i-th point of C-axis of the table is labeled by subscript i. At the tabulation stage, $t_{HR}(C)$ (green line) is first mapped onto the table C-axis, and is discretized in the table as $t_{HR,Tab}(C)$ (black line marked by dots). The time interval between two consecutive points of the tabulated HR time history is then stored at the former point, as $\Delta t_{HR,Tab}(C_i) = t_{HR,Tab}(C_{i+1}) - t_{HR,Tab}(C_i)$; at the table lookup stage, C_{target} is determined by seeking a value that satisfies

$$\Delta t_{Sim} = \sum_{C_i=C(t_0)}^{C_{target}} \Delta t_{HR,Tab}(C_i) \tag{4}$$

Notice that C_{target} is the upper limit of the above summation, and the equality can be tested by incrementally adding the term $\Delta t_{HR,Tab}(C_i)$ into the summation until the desired value of C_{target} is found.

The performance of this tabulation/table lookup strategy of reaction source is tested using homogeneous reaction simulation. Three different types of simulations are carried out: (a) ignition profile is obtained using the tabulated source term and considering it constant over each timestep, (b) integration is performed using the aforementioned strategy that uses the modified tabulation approach, and (c) integration is performed without tabulation but instead by directly integrating ordinary differential equations (ODE) obtained from the chemical mechanism. Figure 4 shows the temperature profile as a function of time for two different unburnt temperatures. A consistent trend is observed: the direct tabulation of reaction source tends to under-predict ignition delay compared to detailed chemistry calculations. This discrepancy can be mitigated by refining the tabulation grid, but even with 500 points in the progress variable space, the results are still not accurate. On the other hand, tabulation/table lookup strategy reproduces the detailed chemistry calculation with only 75 points, which is comparable to conventional requirements for tabulated chemistry [41]. This validates the developed strategy of the direct tabulation of time information instead of reaction rate for ignition simulations.

2.2. FPVA tabulation

The FPVA tabulation is a flamelet-based method for the description of the fully developed flame front [42]. The method assumes what the structure of the flame is, and uses a tabulation approach to impose it in the CFD computation. Specifically, conventional FPVA tabulation solves a family of steady flamelets along

Please cite this article as: Y. Tang, M. Hassanaly and V. Raman et al., A comprehensive modeling procedure for estimating statistical properties of forced ignition, Combustion and Flame, https://doi.org/10.1016/j.combustflame.2019.04.045

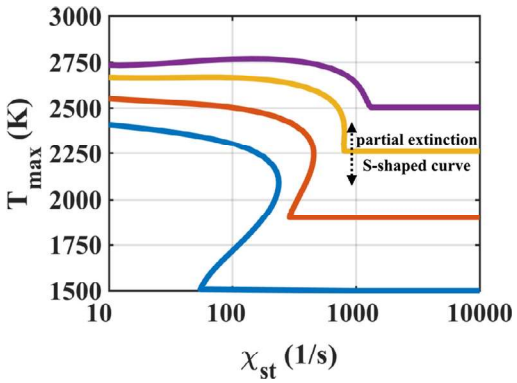

Fig. 5. T_{max} vs. χ_{st} of methane/air counterflow diffusion flamelets obtained at different air stream temperatures ranging from 1500 K to 2500 K. Fuel stream temperature is fixed at 600 K. Operating pressure is 1 atm.

the "S-shaped curve" (in diffusion flame theory) and then maps the resulting solutions onto a lookup table of {*Z*, *C*} [40]. Here, the FPVA tabulation requires an extra mapping variable (total enthalpy *h*) to account for the enthalpy rise due to spark discharge. In this regard, a tabulation strategy similar to that of Mueller [43] is applied, which combines flamelets solved at different enthalpy levels. Counterflow diffusion flamelets are solved here with the boundary temperature of the oxidizer side ranging from room temperature (300 K) to higher levels with increments of 50 K. The flamelet solutions are then mapped onto the phase space of {*h*, *Z*, *C*}.

Note that only the oxidizer temperature is changed to construct the different enthalpy levels. This choice is due to the fact that in this study, the spark originates from the air stream. Further, the presence of a mixing layer that provides entrainment mechanism for flame stabilization is consistent with the diffusion flame structure. The remaining question is to determine until what extent can the temperature boundary be raised until the flamelet solutions can no longer be considered suitable for describing the turbulent flame structure here. While diffusion flamelets with very high-temperature boundary condition are not commonly encountered in FPVA tabulation, a previous study of hydrogen-air counterflow diffusion flamelet [44] found that boundary temperature rise can lead to the partial extinction of flamelet. During partial extinction, the flamelet shows a smooth response of temperature drop to strain rate increments. A similar study is performed here for methane/air reaction and leads to results shown in Fig. 5. It can be seen that the temperature that leads to partial extinction is found to be about 2250 K. Above this temperature, the turning point on the S-shaped curve disappears since the flame is more resistant to strain at higher inflow temperatures. This temperature is used as the upper limit of flamelet calculations. Reaction at a higher enthalpy level will therefore be modeled by HR calculations. The modeling assumptions of this treatment are provided as follows: (a) the boundary temperature that causes partial extinction in the diffusion flamelets is an indication of strong reaction, which supports the approximation of HR. (b) Diffusion flamelet solutions with partial extinction need to be obtained under very large strain rate ($a_{St} = O(10^6)$) in order to get into the extinction region (low progress variable), which simply does not characterize the flow dynamics in this study. In fact, Ref. [44] suggests that flamelets at such high temperature should be applied in flows where the oxidizer stream is influenced by high strain, such as in supersonic combustion. In the present study, the phase space region of high enthalpy and low progress variable should represent a kernel developing toward ignition, instead of a flame front going into partial extinction due to large strain rate.

2.3. Unified FPVA/HR tabulation

In order to be used in a CFD simulation, the two tabulation strategies (HR/FPVA) can be unified into a single lookup table. To build such a table, the progress variable source term of FPVA should be tabulated similarly to the HR tabulation, i.e. in terms of Δt_{Tab}. The progress variable source term $\dot{\omega}_C$ of the diffusion flamelet solutions can be directly mapped onto {*h*, *Z*, *C*}-space, an is called $\dot{\omega}_{C,Tab}$. Along each iso-line of {*h*, *Z*}, Δt_{Tab} can be tabulated using the formula

$$\Delta t_{Tab}(C_i) = \frac{C_{i+1} - C_i}{\dot{\omega}_{C,Tab}(C_i)}. \tag{5}$$

The FPVA $\dot{\omega}_C$ can later be reconstructed during simulation using Eqs. (3) and (4).

Finally, a blended tabulation is needed to model the transition region between HR and FPVA. The enthalpy bounds of the HR and FPVA tabulations are translated from the upper/lower limits of the temperature boundaries applied to populate the HR and diffusion flamelet solutions. This leads to an overlap of enthalpy between the lower bound of HR tabulation and the upper bound of FPVA tabulation. In the unified table, the blended Δt_{Tab} in this region is tabulated as the weighted average of FPVA Δt_{Tab} and HR Δt_{Tab}, with weights that are linearly varying between their respective bounds. While the lower bound of HR tabulation is unambiguously defined by the auto-ignition temperature, the higher bound of FPVA tabulation is based on modeling assumption explained in the last section. In Appendix A, a sensitivity study of the FPVA upper-temperature boundary is performed, where statistical results show that the ignition outcome is insensitive to this boundary.

An example of the unified table is shown in Fig. 6 and illustrates the role of Δt_{Tab}, which may be understood as the inverse of progress variable source term. As the total enthalpy *h* decreases, this ignition time increases as expected. In the FPVA part, the ignition time is very long ($>10^2$ s) when *C* is close to zero, which indicates that a non-burning flamelet cannot be ignited without an external source of enthalpy. Note that the transition between the HR and FPVA regions is smooth, especially for thermophysical properties such as temperature and density, which is important for the stability of the CFD solver.

3. Simulation configuration and numerical setup

In this section, the details of the numerical simulations are provided. Particular emphasis is placed on the choice of boundary conditions to accurately represent the initial spark discharge.

3.1. Experimental configuration

The flow configuration used here is based on the stratified flow facility at the Georgia Institute of Technology [25,32]. The simulation domain is schematically shown in Fig. 7. On the left plane, the inflow is split into two streams by a splitter plate: the kernel flow (air) and the main flow (stratified fuel/air mixture). This configuration is representative of the forced ignition process with fuel stratification effects that typically takes place in aircraft engines during relight. A sunken-fire ignitor is placed at the bottom of the domain, with its top surface aligned with the floor plane. In this experimental facility, the spark is discharged within a cavity recessed from the ignitor top surface, and the thermal expansion inside the cavity forces the kernel to be ejected into the non-reacting "kernel flow" made of pure air (see Fig. 7). The post-discharge kernel then transits through this pure air region and eventually enters the fuel-seeded main flow where chemical reactions can occur. Depending on the initial conditions of the spark and the flow field, the kernel can either dissipate (ignition failure) or sustain and develop into a

Please cite this article as: Y. Tang, M. Hassanaly and V. Raman et al., A comprehensive modeling procedure for estimating statistical properties of forced ignition, Combustion and Flame, https://doi.org/10.1016/j.combustflame.2019.04.045

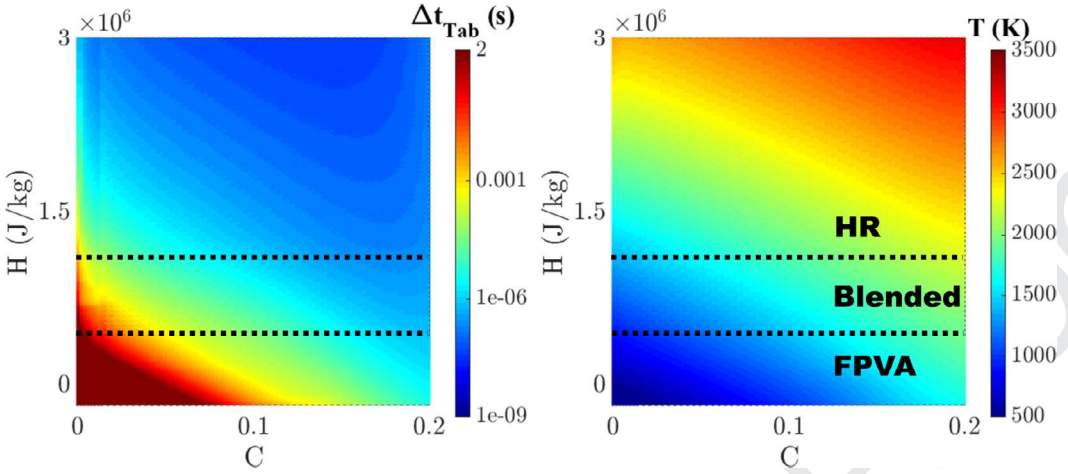

Fig. 6. Unified FPVA/HR tabulation of Δt_{Tab} (left) and temperature (right) in $\{h, C\}$-space, plotted for $Z = Z_{st}$.

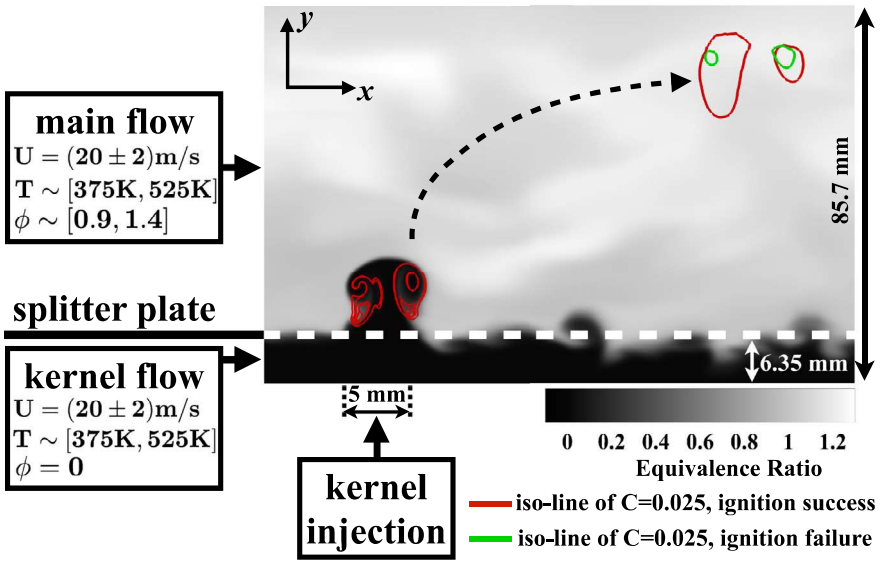

Fig. 7. Schematic of the simulation domain. The cross-sectional area is 54 mm spanwise × 85.7 mm vertical.

stable flame front (ignition success). In this configuration, capturing the transport process of the hot kernel is critical for accurately predicting ignition.

Experimental studies of the facility have been performed with a variety of fuels and operating conditions [1,25,45], which provide measurements of ignition probabilities and information about the ignition physics. A previous numerical study of the configuration has been carried out for Jet-A/air ignition [36], where a preliminary version of the ignition model discussed above was used. In the present work, the goal is to construct a tool that can be used to predict the ignition probabilities of various fuels while handling the multi-dimensional nature of the complex flow field. The target cases contain experiments that explicitly determine the probability of ignition for a range of operating conditions (defined by the ranges of inflow temperature and global equivalence ratio). These cases are listed in Table 1.

In the experimental study, ignition success is defined as a growing kernel at 2 ms after the spark discharge, which is measured by the OH^* signal. This time interval was found to be sufficient to classify most of the possible outcomes [25]. The corresponding numerical definition is detailed in Section 5.4.

Table 1
Experimental operating conditions.

Properties	Values
Pressure	1 atm
Inflow temperature	375–525 K
Fuel/oxidizer	CH_4/air
Main flow global equivalence ratio	0.9–1.4
Kernel flow global equivalence ratio	0
Main/kernel flow velocity	20 ± 2 m/s
Ignitor nominal energy input	1.25 J
Ignitor efficiency	90–95%
Splitter plate height	6.35 mm

3.2. Flow modeling

The turbulent flow is described using the large eddy simulation (LES) framework. Apart from transport equations for the filtered momentum vector, equations for the transport of filtered mixture fraction, total enthalpy, and progress variable are used and are

Please cite this article as: Y. Tang, M. Hassanaly and V. Raman et al., A comprehensive modeling procedure for estimating statistical properties of forced ignition, Combustion and Flame, https://doi.org/10.1016/j.combustflame.2019.04.045

written in a generalized form as follows

$$\frac{\partial \overline{\rho}\widetilde{\Psi}}{\partial t} + \frac{\partial \overline{\rho}\widetilde{u}_i\widetilde{\Psi}}{\partial x_i} = \frac{\partial}{\partial x_i}\left(\overline{\rho}D\frac{\partial \widetilde{\Psi}}{\partial x_i}\right) + \frac{\partial}{\partial x_i}\overline{\rho}\left(\widetilde{u_i}\widetilde{\Psi} - \widetilde{u_i\Psi}\right) + \overline{\rho}\widetilde{\dot{\omega}_\Psi}, \tag{6}$$

where Ψ denotes a scalar. The non-linear closure terms for sub-filter transport are modeled using gradient diffusion hypothesis. A dynamic subgrid scale model [46] is used to obtain the turbulent viscosity. The turbulent diffusivity is obtained using a constant turbulent Schmidt number $Sc_t = 0.72$. A constant turbulent Prandtl number $Pr_t = 0.7$ is used for the energy equation.

The chemical source is obtained based on the tabulation procedure described in Section 2. A presumed-PDF approach is used for the turbulent combustion model. The chemical table is convolved with the joint-PDF of the input variables (i.e., Z, C and h) that describe the sub-filter variations [19,40]. Following prior work [47], the subfilter variations of each variable are assumed independent of each other and the joint-PDF of the input variables becomes the product of three marginal PDF. The marginal PDF of mixture fraction described by a β-function, characterized by the filtered mixture fraction and its variance. The marginal PDFs of C and h are assumed to be described by δ-functions, expressed in terms of the filtered variables. The resulting table contains four input variables (mean and variance of mixture fraction, filtered progress variable and enthalpy).

A low-Mach number solver is utilized here. The LES models are implemented in the OpenFOAM open source code base, which has been specifically modified to minimize kinetic energy dissipation [36,48–51]. A time-staggering approach along with second-order discretization schemes for the convection and diffusion terms are used. The computational mesh for the LES computation consists of 3.9 million grid points, with nearly 15 grid points across the diameter of the ignitor. Grid convergence studies were conducted to ensure that this resolution is adequate for capturing the kernel mixing process.

The effect of the stratified fuel that enters the main flow heavily rely on the turbulence statistics at the inlet of the domain. To ensure that the turbulent flow is properly represented, auxiliary cold flow simulations of the upstream mixing process are conducted and serve as time-dependent boundary conditions for the main and kernel flow. Details of these simulations and their validation against experimental data are provided in [36]. The auxiliary simulation data are stored at a frequency corresponding to twice the turnover time of the smallest resolved eddy, determined by the local velocity and filter width. These simulations provide inflow conditions for all field variables except enthalpy. The enthalpy inflow boundary conditions are inhomogeneous and time-dependent since they depend on the local equivalence ratio and inflow temperature. The inlet boundary condition for enthalpy is dynamically updated during the simulations using the lookup table.

3.3. Modeling of spark discharge

One of the key sources of ignition variability (i.e., success or failure to ignite) is the inherent stochasticity associated with the spark discharge process. In this work, the modeling process consists of (a) using a sufficiently descriptive kernel injection to replicate the necessary flow physics, and (b) treating other sources of variability as uncertainty. The details of the modeling are provided below.

The experimental ignitor uses a spark discharge to create the initial kernel. Due to the high temperature within this kernel, nonequilibrium thermal effects including the formation of plasma are possible [11]. However, these conditions then quickly form an equilibrium state. For instance, this intense energy release causes the kernel that ejects from the ignitor to be preceded by a weak shock wave, which dissipates in $\mathcal{O}(1\ \mu s)$ [11]. Similarly, the time scale for the plasma to recombine into electrically neutral species occurs over $\mathcal{O}(50\ \mu s)$ [31]. These two time scales are small compared to the time needed for the kernel to be transported from the kernel flow to the main flow ($\mathcal{O}(125\ \mu s)$) [31]. Therefore the shock wave is neglected, and the spark discharge is treated solely as an energy input. Moreover, the thermal expansion following the spark discharge within the ignitor cavity can also be excluded from the simulation. Instead, the simulation of the post-discharge kernel is modeled as a pulse-jet-in-crossflow (PJICF) introduced from the boundary of the ignitor top surface. The gas phase properties of the kernel are estimated using a 0-D analysis of the expansion process [25], and the necessary details are presented below.

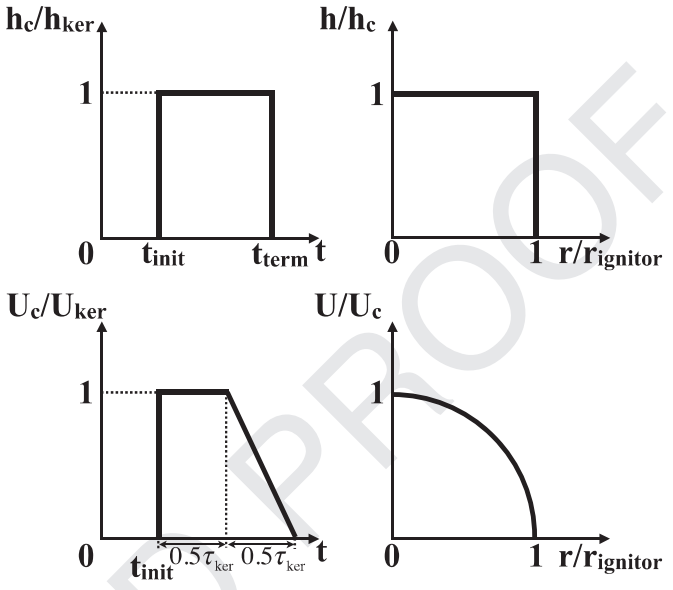

Fig. 8. Temporal (left) and spatial (right) profiles of total enthalpy (top) and normal velocity (bottom) applied at the kernel boundary. Subscript 'c' denotes value at the boundary center, and 'ker' denotes the bulk value.

At the kernel injection boundary (Fig. 7), velocity and enthalpy are specified using time-dependent Dirichlet conditions. Note that the kernel is made of air at an elevated temperature and does not contain fuel. The applied temporal and spatial profiles are summarized in Fig. 8 where h_{ker} and U_{ker} are respectively the characteristic value of the kernel enthalpy and velocity, t_{init} is the time at which the enthalpy and velocity boundary enforcement starts, t_{term} is the time at which the enthalpy boundary enforcement ends, $\tau_{ker} = t_{term} - t_{init}$ is the duration of the velocity boundary enforcement, and $r_{ignitor}$ is the radius of the ignitor top surface. This functional form for boundary conditions is adopted so that the trajectory of individual kernels reasonably approximates the experimental observations.

A uniform spatial profile is used for the kernel enthalpy boundary, where the characteristic value h_{ker} is linearly related to the spark deposit energy E_d by 0-D energy conservation as

$$h_{ker} = h_0 + \frac{E_d}{\rho_0 V_{cav}}. \tag{7}$$

E_d measures the energy deposited into the gas phase during the spark discharge. This value cannot be exactly controlled and is considered a random variable for the uncertainty quantification (described in Section 5.3. E_d is related to E_n which is the nominal electrical energy of the discharge arc. In this case $E_n = 1.25\ J$ [25]. The deposition efficiency which is the ratio of E_d to E_n was assumed to be 90–95% due to the short discharge duration [25,52].

Please cite this article as: Y. Tang, M. Hassanaly and V. Raman et al., A comprehensive modeling procedure for estimating statistical properties of forced ignition, Combustion and Flame, https://doi.org/10.1016/j.combustflame.2019.04.045

h_0 and ρ_0 are the pre-discharge flow properties. The volume of the ignitor cavity V_{cav} is 0.2 cm^3 (Sheng, personal communication, October 2017). Notice that Eq. (7) assumes that all the cold flow located within the ignitor cavity is entrained into the kernel. This is in line with the study by Sforzo using partially stirred reactor modeling, where it is found that the volume of cold flow within the ignitor cavity is estimated to be $\mathcal{O}(0.1)$ cm^3 to achieve the correct initial state of the kernel. The kernel enthalpy boundary follows a step profile, which is initiated when a spark discharge is triggered. The time duration is set such that a prescribed mass of fluid enters the domain, which is controlled by V_{ker}, the volume of the kernel. This quantity is also difficult to control in the experiments, and only estimates are available [1,25,52]. Here, the order of $\mathcal{O}(0.25$ $cm^3)$ [52] is applied, which was found to best reproduce the initial kernel diameter compared to Schlieren measurements [25]. Last, while the spark discharge is characterized by E_d, it is clarified that with the above boundary conditions, the total energy injected into the domain ($h_{ker}\rho_{ker}V_{ker}$) is actually lower than E_d due to the ratio between $\rho_{ker}V_{ker}$ and $\rho_0 V_{cav}$. This relation is supported by a recent study that provides more accurate measurements on the kernel initial properties created by this particular igniter [53].

The velocity boundary condition consists of two parts (see Fig. 8). The velocity at the center of the injector U_c is obtained from a trapezoidal profile that depends on a nominal kernel velocity U_{ker}. A spatial parabolic profile is then applied across the injector diameter. The kernel injection duration and velocities are again subject to uncertainty but are $\mathcal{O}(50$ $\mu s)$ and $\mathcal{O}(300$ m/s), respectively, in order to reproduce the observed kernel shapes and trajectories [25].

In summary, the kernel injection is fully specified by four parameters $K = \{E_d, V_{ker}, \tau_{ker}, U_{ker}\}$. The uncertainty of the initial spark discharge can therefore be represented as uncertainties for these parameters. The approach for treating these uncertainties will be discussed separately in Section 5.3. In order to demonstrate the validity of the chosen set of parameters, a nominal simulation has been performed in Appendix B, which reproduced the time sequence of kernel shape and locations reasonably well. In the following discussions, this injection approach as well the flow models described above will be used.

4. Physics of kernel ignition process

Using the models described above, the essential physics of ignition are discussed in this section. The objective is to elucidate the fundamental physics of kernel transport, specifically its mixing process with the fuel seeded flow.

4.1. Dynamics of main flow-kernel mixing

Prior studies of PJICF [54] showed that the kernel evolution is strongly dependent on the formation of vortex rings at the leading edge of the jet. The structure of these rings depends on non-dimensional parameters given by the velocity ratio ($r = U_{ker}/U_{main}$) and stroke ratio ($L/D = U_{ker}\tau_{ker}/(2r_{ignitor})$). For the current study, U_{ker} is set to 300 m/s, τ_{ker} is set to 50 μs, which leads to $r = 15$ and $L/D = 3$. Under these conditions, the PJICF displays discrete vortex rings [54], which is seen in Fig. 9. The vortex ring has a short trailing vortex column, the length of which is directly proportional to stroke ratio. The vortex ring is tilted upstream, with the leeward vortex rising faster than the windward component. This horizontal momentum comes from the Kutta–Joukowski lift that is induced by the relative velocity between the crossflow and vortex circulation. The evolution of these vortex rings was found to have a clear impact on mixing in prior studies [54], and is observed here as well. To understand the mixing process, the transient behavior of the mixture fraction field is also shown in Fig. 9. The vortex entrains fuel as it rises through the main flow. After $t = 0.46$ s, the leading edge splits into two vortices where additional stretching and molecular mixing occur. At later times, the distinct vortex shape is lost, and the fuel–air mixing process is sufficiently complete, at least near the leading edge of the kernel.

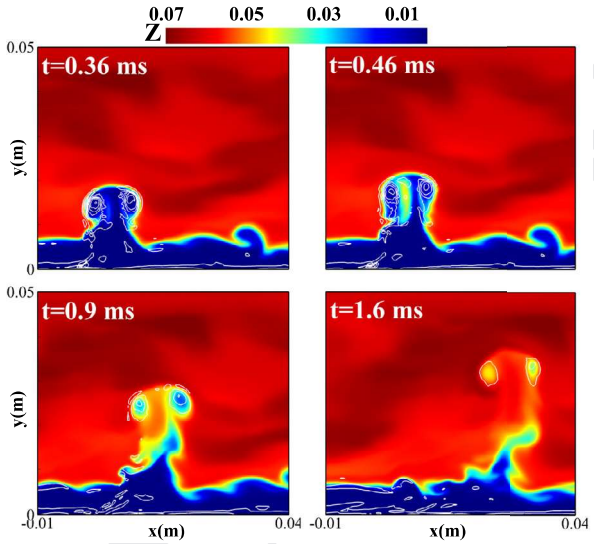

Fig. 9. Time series of vortex evolution and scalar mixing for a kernel PJICF of ignition success plotted at the mid-plane in spanwise direction. White line – contour lines of out-of-plane vorticity ω_z; colored contour – mixture fraction Z. (For interpretation of the references to color in this figure legend, the reader is referred to the web version of this article.)

4.2. Ignition mechanisms of the kernel PJICF

In this section, the physical process of a successful or failed ignition is described. For this purpose, two different simulations are used. Both cases use the same initial flow field, kernel size $V_{ker} = 0.275$ cm^3, and kernel velocity $U_{ker} = 300$ m/s. However, the spark deposition energy is varied for the two cases by 0.8%, with $E_d = 1.2325$ J and 1.2425 J, respectively. These values are chosen by trial and error to represent the separation between success and failure of ignition. Note that when all other parameters are held constant, there is a clear separation between the ignition and failure regimes for each of the input variables. In other words, these events are deterministic for any given set of parameters.

Figures 10 and 11 show the time evolution of an iso-surface of progress variable for the successful and failed ignition cases, respectively. For the successful case, and at early times (before 0.9 ms), the reaction front has a complex spatial structure. For reference, Fig. 9 discussed above corresponds to this case. It can be seen that the progress variable peaks along a vertical column that goes through the vortex ring of the kernel. At later times (after 1.6 ms), it can be seen that the ignition occurs along the outer edge of the kernel, in regions where entrainment of the fuel–air mixture into the kernel flow is complete. The reaction front then propagates gradually to the leeward side. For the failed ignition case, the progress variable iso-surfaces are noticeably smaller after $t = 0.9$ ms. This shows that the reaction has already been inhibited enough even before this time. After $t = 1.6$ ms the horseshoe-shape pattern is not visible and the reaction zone gradually dissipates until complete disappearance at $t = 3.5$ ms.

To further understand the details of ignition, a Lagrangian analysis is conducted. A set of tracer particles are seeded in the flow, and the gas-phase properties seen by these particles are recorded

Please cite this article as: Y. Tang, M. Hassanaly and V. Raman et al., A comprehensive modeling procedure for estimating statistical properties of forced ignition, Combustion and Flame, https://doi.org/10.1016/j.combustflame.2019.04.045

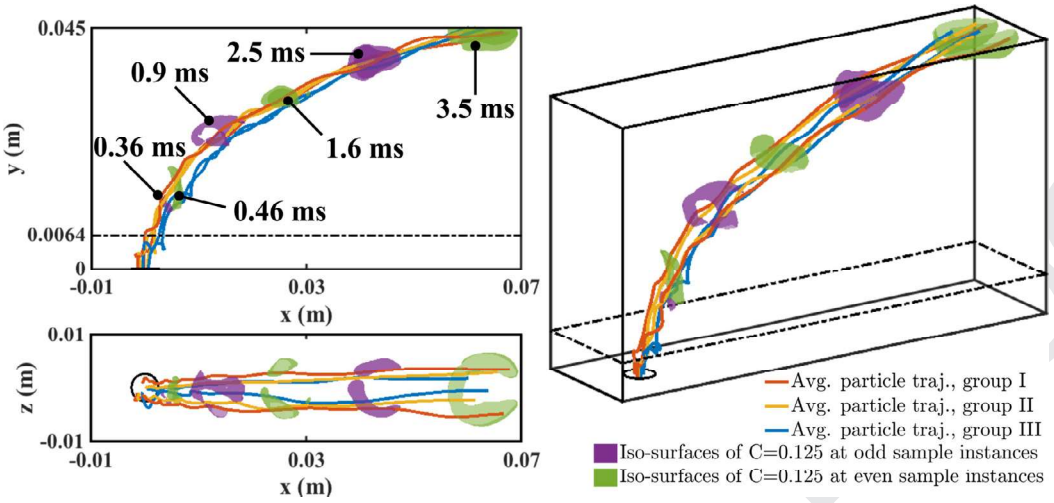

Fig. 10. Time series of a successful ignition kernel development: averaged fluid particle trace lines conditioned on the ignition final states at $t = 3.5$ ms. Group I: $C \geq 0.125$; Group II: $0.05 \leq C \leq 0.125$; Group III: $C \leq 0.05$. Iso-surfaces of progress variable C sampled at 6 time instances. Dash line estimates the location of the mixing layer.

as they move within the domain. The particles are grouped based on their recorded progress variable at an end time, taken to be $t = 3.5$ ms here. The trajectories of fluid particles grouped by the end state show interesting features. It is seen that the primary contributor for ignition success is the formation of the kernel vortices as the pulsed-jet turns into the crossflow. In the failed ignition case, this outer region of highly reacted gases fails to stabilize.

The side-view of the trajectories shows another feature. The igniting part of the kernel is positioned towards the windward side, which is consistent with the kernel vortex formation that is stronger on this side than the leeward side that is protected by the jet itself from the crossflow. As a result, Group I trajectories are found on the windward side, while the non-igniting Group III trajectories are on the leeward side. For the failed ignition case, there is not much variation in the trajectories of the different groups. This clearly indicates that the entrainment mechanism that produces the ignition pockets has failed to stabilize the reaction zone. As a result, fluid particles on the windward side also fall in the III group. Note that all the trajectories only present an averaged result of the particle behaviors.

The different trajectory groups can be plotted in the $\{C, h\}$ space as shown in Fig. 12. All the groups follow similar trajectories up to $t = 0.9$ ms, which is the time it takes for the kernel to reach the diffusion-controlled ignition region dominated by the FPVA model. At this stage, the different trajectories diverge, with the non-igniting group moving towards low C values, consistent with a failure to ignite. The igniting group moves towards high C values, indicating that the increase in temperature has been sustained long enough to reach a stable burning solution. The middle group (Group II in the plot) exhibits a non-monotonic trend. In the successful ignition case, it can be seen that this group first moves towards extinction, but appears to be stabilized later on. This group is hence a marker of the kernel ignition process, with failed kernels pushing these trajectories towards lower C values.

The ignition process can also be described in terms of the kernel volume, marked by region of high progress variable values. For this purpose, the volume of fluid occupied by different progress variable groups can be tracked as a function of time. Since values greater than zero are feasible only within the kernel volume, the sum of all of these group volumes will provide the total kernel volume. Figure 13 shows the evolution of the group volumes for the two cases. The group with progress variable in the range of [0.05,0.125] is formed predominantly by entrainment and sig-

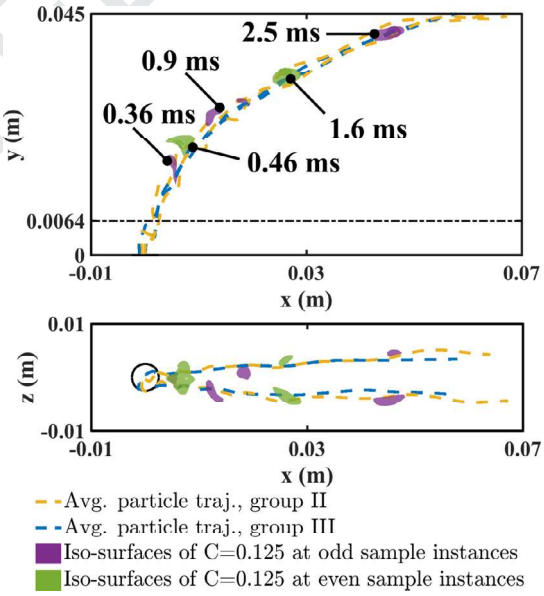

Fig. 11. Time series of a failed ignition kernel development plotted in the same fashion as in Fig. 10. Group I does not exist here as no particles achieved final ignition.

nals the initial region of ignition. For both cases, this volume grows with time until $t = 0.9$ ms, which is the time when these groups reach the diffusion-limited reaction part of the process. It is seen that at this stage, excessive straining can quickly quench this initial ignition pocket. On the other hand, the successful ignition process is able to make the transition to a diffusion-controlled flame, which is accompanied by an increase of the flow volume with progress variable > 0.125. As this high progress variable region grows in volume, it infuses higher enthalpy to the inner part of the kernel, causing a growth in the volume of the $C = [0.05, 0.125]$ group as well.

As an intermediate conclusion, the detailed ignition model used in this work is able to capture ignition success and failure, and is sensitive to input parameters such as the deposition energy. However, to compare directly with experiments, a more rigorous uncertainty quantification framework needs to be built around this LES-based approach, and is discussed next.

Please cite this article as: Y. Tang, M. Hassanaly and V. Raman et al., A comprehensive modeling procedure for estimating statistical properties of forced ignition, Combustion and Flame, https://doi.org/10.1016/j.combustflame.2019.04.045

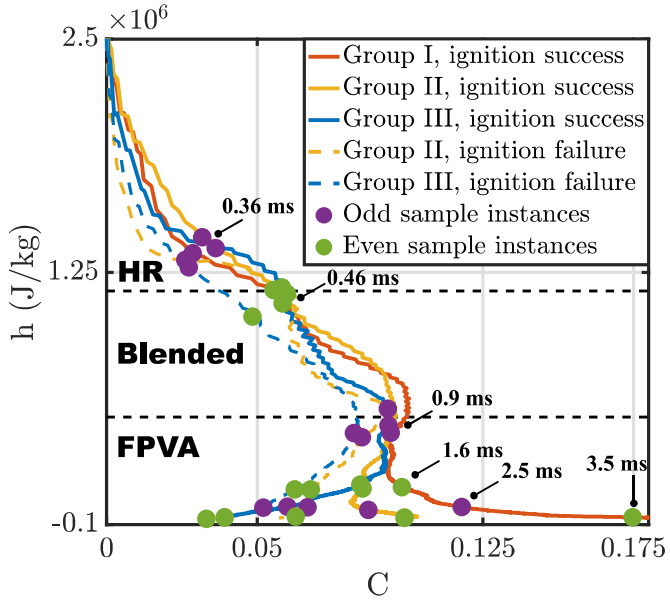

Fig. 12. Averaged particle trajectories plotted in $\{h, C\}$-space. Dots mark the positions on the trajectories that correspond to the sampled instances in Figs. 10 and 11. Dash lines indicate the boundaries between the three regions applied in the developed ignition tabulation.

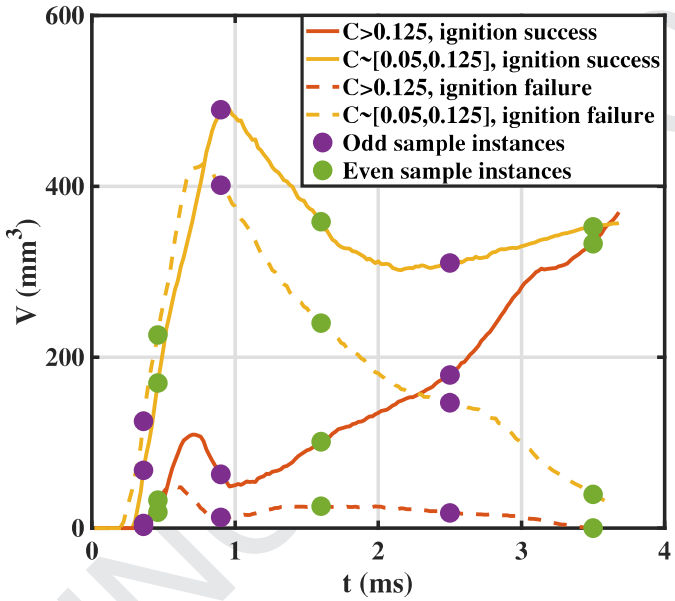

Fig. 13. Time history of grouped volumes. Dots mark the sampled instances same as in Figs. 10 and 11.

5. Estimating ignition probability using uncertainty quantification approach

Ignition is heavily influenced by inherent variabilities in the spark deposition process and the turbulent flow that mediates this process. It is then natural to consider ignition probability, which is essentially the probability that ignition success will occur for a set of macroscopic nominal conditions that may have spatial and temporal variations. In this particular study, the global equivalence ratio of the main flow and its temperature are considered as the defining macroscopic variables. Two sets of experiments, one with varying equivalence ratio and the other with temperature changes, are available for validation. In general, the estimation of such variabilities is carried out using uncertainty quantification (UQ) approaches [19,20,55].

Very simply, these approaches use a Monte-Carlo type method that treats the variabilities as arising from a known probability distribution, and conducting an ensemble of computations with parameter values sampled from this distribution. Since the underlying LES calculations are computationally intensive, it is necessary to determine the most important sources of variability so as to limit the size of the ensemble. In this section, these issues and the resulting UQ procedure is described.

5.1. Formulation of uncertainty problem

The uncertainty in ignition comes from the kernel parameters K and the state of the initial turbulent flow field ξ. This latter quantity is a high-dimensional vector that describes the initial velocity and scalar fields at the M grid points used to solve the LES fields. The probability of ignition can be formally expressed as

$$P_{Igni}(O) \triangleq E(I(K,\xi;O)) = \iint I(K,\xi;O) f_{K,\xi}(K,\xi;O)\, d\xi\, dK, \tag{8}$$

where O denotes the parameters that define the operating conditions (main flow temperature T and main flow global equivalence ratio ϕ), E is the expectation operator (average over a statistical distribution), I is an ignition indicator function ($I = 1$ for a successful ignition and $I = 0$ for a failure case), $f_{K,\xi}$ is the joint probability density function (PDF) of K and ξ. Here, K and ξ are vectors of random variables, while O is treated as non-random parameter that affects the shape of the joint-PDF $f_{K,\xi}$. The inner integration of the joint PDF in Eq. (8) can be further replaced conditional ignition probability, as

$$P_{Igni}(O) = \int P_{Igni|K}(K;O) f_K(K)\, dK, \tag{9}$$

where $P_{Igni|K}(K;O) = \int I(K,\xi;O) f_\xi(\xi|K;O)\, d\xi$, and $f_K(K)$ is the PDF of K that is assumed to be known and independent of the operating conditions and the local turbulence properties. This assumption is physically justified as the kernel properties mostly depend on the ignitor, more so than the flow field.

In short, the computational strategy is to first determine the probability due to the impact of turbulence on a particular choice of kernel parameters K, and then compute final ignition probability by convolving the result with the PDF of kernel parameters K. The former probability is approximated using an empirical mean of the value of the ignition indicator obtained from multiple simulations as

$$P_{Igni|K}(K;O) = \frac{1}{N}\sum_{\xi\in\Xi} I_{Sim}(\xi;K,O) + \varepsilon_{Spl}(K,O) = P_{Igni|K,Spl}(K,O) + \varepsilon_{Spl}(K,O), \tag{10}$$

where N is the number of samples used to compute the empirical mean, Ξ is the ensemble of N initial turbulent flow fields used in the empirical mean, I_{Sim} is the ignition indicator value (1 or 0) obtained from each LES simulation, $P_{Igni|K,Spl}(K, O)$ is the estimator of $P_{Igni|K}(K; O)$ and $\varepsilon_{Spl}(K, O)$ is the statistical sampling error. The choice of N used to estimate the turbulence-induced variability is discussed further in Section 5.2, and the impact of $\varepsilon_{Spl}(K, O)$ on the computed probability is discussed in Section 5.6.

The above approach provides a convenient path to evaluating the effect of the high-dimensional turbulent flow field while providing a functionally smooth probability function rather than a binary indicator function. This latter feature is especially useful in the determination of the ignition probability (P_{Igni}) using the polynomial chaos expansion (PCE) approach.

Please cite this article as: Y. Tang, M. Hassanaly and V. Raman et al., A comprehensive modeling procedure for estimating statistical properties of forced ignition, Combustion and Flame, https://doi.org/10.1016/j.combustflame.2019.04.045

5.2. Sampling turbulent flow field

The sampling of turbulence to represent the correct density function is a computationally expensive problem. To be precise, the statistically stationary flow without the kernel discharge subscribes to an attractor in high-dimensional space [56,57]. In order to obtain the correct density of initial conditions, points on this attractor need to be sampled. It is known that even for low Reynolds number flows, the dimension of this attractor can be sufficiently large that such a direct sampling will be expensive [19,56,57]. In this study, it is assumed that the fully developed main and kernel flow (the crossflow) moves on an attractor, and starting the ignition calculations at different initial times is equivalent to sampling the attractor. This assumption is valid for ergodic systems [58].

In practice, the simulations are started from the same initial conditions, but the time at which the spark kernel is discharged is varied to produce different initial states for the kernel propagation environment. A total of $N = 15$ simulations are conducted for each kernel parameter set, with the start time between the initial states varying by 10 ms. As a comparison, the flow time-scale where turbulence controls kernel evolution is the time taken by the kernel to traverse the kernel air. This time-scale is $\mathcal{O}(0.1)$ ms based on nominal injection velocity and the distance between the main flow and the injection location. For each set of kernel parameters and operating conditions, N such simulations are used to estimate $P_{Ign|K}$. For the present studies, $N = 15$ was found to be adequate.

5.3. Impact of the kernel parameters on ignition

While the kernel model uses a set of parameters defined by $K = \{E_d, V_{ker}, \tau_{ker}, U_{ker}\}$. not all of these parameters are uncorrelated. In order to minimize the phase-space of uncertain variables, it is useful to consider these correlations to limit the parameter set. As a starting point, consider E_d and U_{ker}. While it can be postulated that increasing the deposition energy will increase the probability of ignition, the dependence of the ignition event on U_{ker} is less direct. For instance, higher velocities will cause the kernel to reach the main flow faster, but will also increase kernel air entrainment leading to dissipation of the high-enthalpy gases. To further understand the relative roles of these parameters, a series of cases varying $\{E_d, U_{ker}\}$ within two standard deviations of their nominal values of {1.24 J, 300 m/s} is conducted. These standard deviations are set to {0.02 J, 25 (m/s)}, based on results from [25]. When all other conditions are maintained the same, the results in Fig. 14 is obtained. The model captures the impact of the velocity of the kernel as well as its energy on the ignition outcome. The energy of the kernel primarily influences the ignition outcome. Moreover, the variation in critical energy for ignition is nearly constant for a wide range of velocities, indicating that spark energy deposition is the dominant factor. While there is considerable uncertainty in the specification of injection time and kernel volume, the previous section (Section 3.3) used experimental images to calibrate these values. Here, it is assumed that post-calibration, the uncertainty in these parameters is small. As a result, any uncertainty in the kernel parameters is reduced to uncertainty in E_d. In the following paragraphs, the subscript K is replaced by the subscript E_d.

5.4. Simulation conditions for sampling procedure

The set of discrete operating conditions simulated here is provided in Table 2 and is decomposed in O_T and O_ϕ, where O_T denotes the set operating conditions tested at fixed global equivalence ratio but variable main flow temperature, and O_ϕ denotes the set operating conditions tested at fixed main flow temperature but variable global equivalence ratio. The objective is to determine the ignition probability as a function of either the main flow temperature or global equivalence ratio. In order to estimate I_{Sim} in Eq. (10), a particular simulation is considered ignition success if the kernel volume, measured as the total volume of computational cells with temperature higher than 1500 K, increase from 2 ms to 3 ms after the spark. This definition is consistent with the experimental study detailed in Section 3.1.

For the purpose of this study, the kernel deposition energy is varied between 1 and 1.6 J, where the kernel ignited/failed at the upper/lower limit with probability 1. Using 15 sampling times for the turbulent flow and 60 levels for spark energy density, a total of 900 simulations is required for each operating condition. Given that there are 9 independent operating conditions, the total number of simulations can quickly become expensive or even intractable for more complex problems. In order to further reduce the computational cost, the monotonic behavior of ignition due to variation in spark energy density is used. As shown in Fig. 14, there is a clear dependence on energy density. Essentially, the objective is to find the bifurcation energy, which separates ignition failure from success. The bisection method employed here is shown in Table 3. Here, for each operating condition and turbulence sampling time, different realizations with varying spark energy densities are considered. Moving from the nominal value towards higher and lower values, the ignition failure or success is noted. As the energy density is increased, if two successive realizations produce successful ignition, then higher ignition energies need not be considered since they will produce successful ignition as well. In this manner, the average number of realizations required for each turbulence sampling time and operating condition was reduced to approximately 6 as opposed to 60, providing an order of magnitude decrease in computational cost. Using this approach, the total computational time for the 803 realizations simulated on 1008 processors is approximately 10^6 core hours.

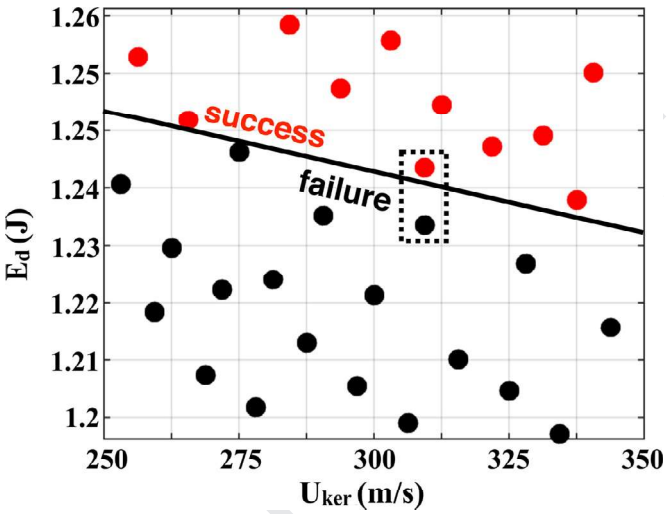

Fig. 14. Points in the $\{E_d, U_{ker}\}$-space tested in the parameter study colored by their ignition outputs: red – successful ignition; black – failed ignition. Dashed box indicates the two cases that were applied for in-depth analysis in Section 4.2. (For interpretation of the references to color in this figure legend, the reader is referred to the web version of this article.)

Table 2
Simulation operating conditions T refers to the temperature of the main flow while ϕ is the global equivalence ratio of this stream.

	T (K)	ϕ
O_T	375, 425, 455, 485, 525	1.1
O_ϕ	455	0.9, 1.1, 1.2, 1.3, 1.4

Please cite this article as: Y. Tang, M. Hassanaly and V. Raman et al., A comprehensive modeling procedure for estimating statistical properties of forced ignition, Combustion and Flame, https://doi.org/10.1016/j.combustflame.2019.04.045

Table 3
Demonstration of the sampling procedure of the conditional ignition probability $P_{Igni|E_d,Spl}$. The ignition outputs marked by circle are directly obtained from simulation outputs, while the rest are set to 0 or 1 by assuming that I_{Sim} monotonically increases with E_d.

t_{Spk}	E_d (J)				
	1.2	1.21	1.22	1.23	1.24
t_0	0	⓪	①	1	1
t_1	⓪	①	①	1	1
t_2	0	0	⓪	⓪	①
t_3	0	0	⓪	①	1
t_4	0	⓪	①	1	1
$P_{Igni|E_d,Spl}$	0	0.2	0.6	0.8	1.0

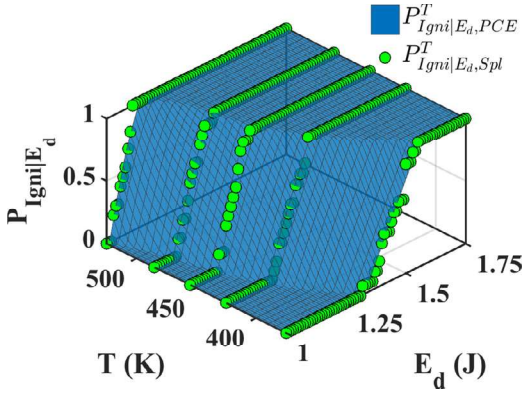

Fig. 15. Response surface of conditional ignition probability $P^T_{Igni|E_d,PCE}$ in $\{E_d, T\}$-space, plotted along with the sampled ignition probability $P^T_{Igni|E_d,Spl}$ based on which the PCE was performed.

5.5. Response surface of ignition outcome

One of the challenges with the sampling approach described above is that the numerical results are discrete in nature, providing outcomes for discrete values of kernel parameters and operating conditions. However, to convolve the probability computed with the probability of the kernel properties, the output of the model should be made continuous. Here, $P_{Igni|E_d,Spl}$ needs to be represented as a continuous function of the sampling parameters and operating conditions. For this purpose, so-called response surfaces are constructed in the phase space of $\{E_d, T, \phi\}$, which provides a continuous surrogate of the discretely sampled $P_{Igni|E_d,Spl}$. Here, two different response surfaces are constructed to represent $P^T_{Igni|E_d,Spl}(E_d, T)$ (probability of ignition computed at variable main flow temperature) in the space $\{E_d, T\}$ and $P^{\phi}_{Igni|E_d,Spl}(E_d, \phi)$ (probability of ignition computed at variable global equivalence ratio of the main flow) in the space $\{E_d, \phi\}$. The response surfaces are constructed using polynomial chaos expansion (PCE) [20,59], which traditionally is used to represent a random variable as a linear combination of polynomials of other random variables. Here, it is used to represent a random variable (the probability of ignition) as a function of one random variable (E_d) and one deterministic variable (T or ϕ). E.g., for $P^T_{Igni|E_d,Spl}(E_d, T)$, as

$$P^T_{Igni|E_d,Spl}(E_d, T) = P^T_{Igni|E_d,PCE}(E_d, T) + \mathcal{R}^T_{PCE}(E_d, T), \tag{11}$$

where the output of PCE is denoted by the subscript "PCE", and $\mathcal{R}^T_{PCE}$ is the residual of the expansion. The construction of $P^T_{Igni|E_d,Spl}(E_d, T)$ is included in Appendix C.

Figures 15 and 16 show the response surfaces for the two different sets of operating conditions. It is seen that the resulting surface are smooth due to the polynomial representation even if the actual data points exhibit variabilities due to statistical errors. For the response surface approximating $P^{\phi}_{Igni|E_d,Spl}$, the ignition probability profile has an inflection point around $\phi = 1.2$ where even low spark energy values are able to sustain ignition.

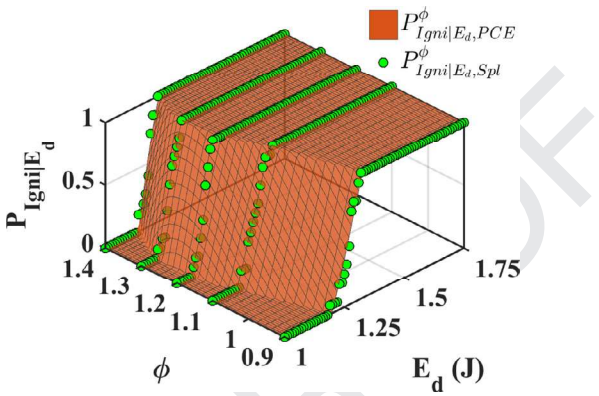

Fig. 16. Response surface of conditional ignition probability $P^{\phi}_{Igni|E_d,PCE}$ in $\{E_d, \phi\}$-space, plotted along with the sampled ignition probability $P^{\phi}_{Igni|E_d,Spl}$ based on which the PCE was performed.

5.6. Estimation of sampling and polynomial truncation errors

Based on the response surface constructed using the sampled data and the PCE approach, a modeled conditional ignition probability $P^T_{Igni|E_d,PCE}$ can be obtained. Since this quantity is subject to both sampling error (due to finite number of samples) and the PCE truncation (due to finite number of polynomials), the true conditional ignition probability can be written as

$$P^T_{Igni|E_d}(E_d, T) = P^T_{Igni|E_d,PCE}(E_d, T) + \mathcal{R}^T_{PCE}(E_d, T) + \varepsilon^T_{Spl}(E_d, T), \tag{12}$$

which is obtained by combining Eqs. (10) and (11). The two errors are specified here in two different ways. The sampling error ε^T_{Spl} is the continuous statistical convergence error due to to the sampling of turbulent realizations in the $\{E_d, T\}$ space, and defined in the same manner as ε_{Spl}. Using the central limit theorem, ε^T_{Spl} can be assumed normally distributed with zero mean and a variance $\sigma^2_{\varepsilon^T_{Spl}}$ that can be approximated as:

$$\sigma^2_{\varepsilon^T_{Spl}}(E_d, T) = \frac{P^T_{Igni|E_d,PCE}(E_d, T)(1 - P^T_{Igni|E_d,PCE}(E_d, T))}{N}, \tag{13}$$

where N is the number of samples used to estimate the conditional ignition probability for a given kernel energy density. In this study, this sampling error is only due to the turbulence sampling, and N denotes the number of turbulence starting profiles used as described in Section 5.2. Similar derivations can be done with the operating conditions at variable global equivalence ratio of the main flow and $\sigma^2_{\varepsilon^{\phi}_{Spl}}$ can be obtained in the same manner. A contour of the resulting $\sigma_{\varepsilon^{\phi}_{Spl}}$ is shown in Fig. 17. Compared with Fig. 16, it is seen that sampling error is highest near the region where ignition probability increases from 0 to 1 (the bifurcation point). Based on the parameters used here, the peak standard deviation is around 0.13.

The residual error term from the PCE expansion is of a fundamentally different nature than the statistical sampling error, in that it arises from the finite-term truncation of the polynomials. An evaluation of this error is performed in Appendix C. The conclusion is directly applied here, that the residual error stemming

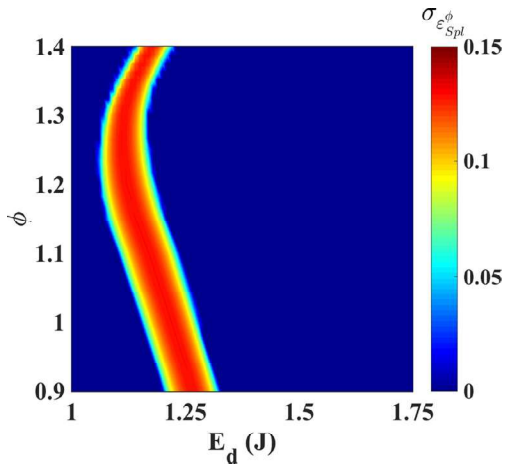

Fig. 17. Contour of the standard deviation of the statistical sampling error plotted in $\{E_d, \phi\}$-space.

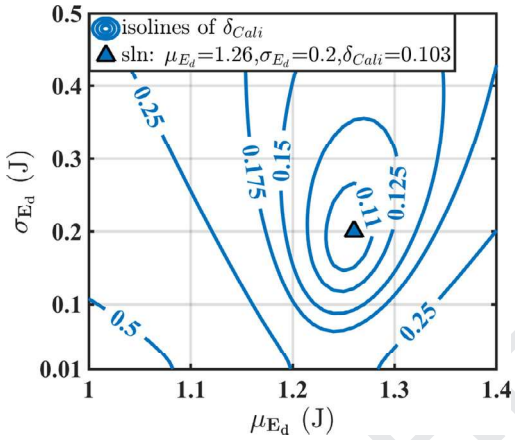

Fig. 18. Contour of total error between convolved ignition probability and experimental measurement calibrated with the experimental dataset at variable main flow temperature but constant global equivalence ratio.

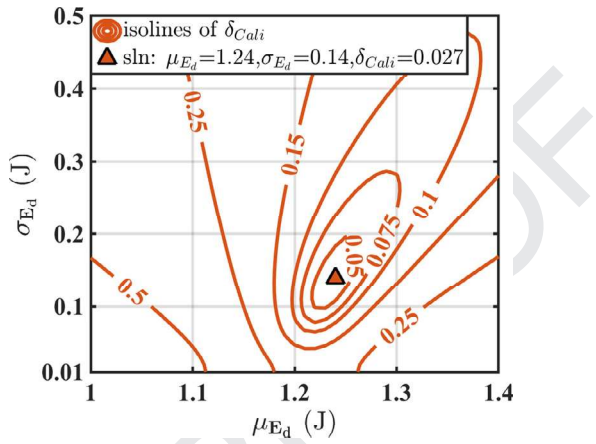

Fig. 19. Contour of total error between convolved ignition probability and experimental measurement calibrated with the experimental dataset at variable global equivalence ratio but constant temperature.

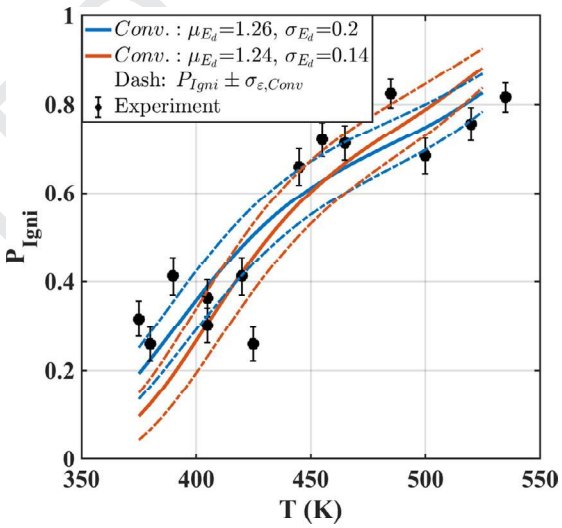

Fig. 20. Comparison of the final probability of ignition $P_{Igni}(T, \phi = 1.1)$ convolved with two sets of calibrated coefficients of $\{\mu_{E_d}, \sigma_{E_d}\}$. The calibration was done with the experimental dataset at variable main flow temperature (blue line) and the experimental dataset at constant global equivalence ratio (red line). (For interpretation of the references to color in this figure legend, the reader is referred to the web version of this article.)

from the PCE truncation is negligible compared to the sampling error, and therefore discarded in the results discussed below.

5.7. Ignition probability estimation

The conditional ignition probability has taken into consideration variabilities in turbulent flow and provided a function that only depends on one random variable: the spark deposit energy. Since this energy is not precisely known, the probability of ignition is obtained by convolving the conditional ignition probability with the distribution of spark kernel energies (Eq. (9)), which provides a measure of ignition odds for a given set of operating conditions.

Of course, the primary challenge here is to specify the kernel energy distribution. This is not a measurable quantity and needs to be estimated or calibrated based on experimental data. One approach to determining these uncertain distributions is the Bayesian technique [19,20,55]. Here, instead of using a full-blown Bayesian formulation, the spark energy uncertainty is assumed to be normally distributed with a mean and variance. Further, the likelihood function is also assumed to be Gaussian which leads to a posterior that is normally distributed as well. Since only a single uncertain variable is involved, linear regression estimates are sufficient to determine the posterior distribution. The regression-based estimation is obtained with subsets of experimental data; that is, either the uncertainty is determined based on the equivalence-ratio or temperature variation experiments, and the result validated using the remaining experimental data.

For the discussion below, the regression error is determined as the L_2-norm of error between ignition probability from experiments and that obtained from Eq. (9). Figure 18 shows this error for different values of mean energy (μ_{E_d}) and standard deviation (σ_{E_d}) of the spark energy distribution, calibrated using experiments that contain variations in main flow temperature but at constant equivalence ratio. It is seen that the mean value that minimizes error is close to 1.25, which is the nominal energy deposited by the ignitor. It is also seen that as the mean value is varied, the error increases even if the standard deviation is changed significantly. As a result, the set of mean and standard deviation that leads to the lowest error is considered the calibrated mean and standard deviation for the distribution of kernel energies. A similar procedure can be carried out using the experimental data involving variations in equivalence ratio but at constant main flow temperature, and is shown in Fig. 19. Here again, the calibrated mean value of energy deposition is close to the nominal value. However, the standard deviation is slightly different, changing from 0.2 in the constant ϕ

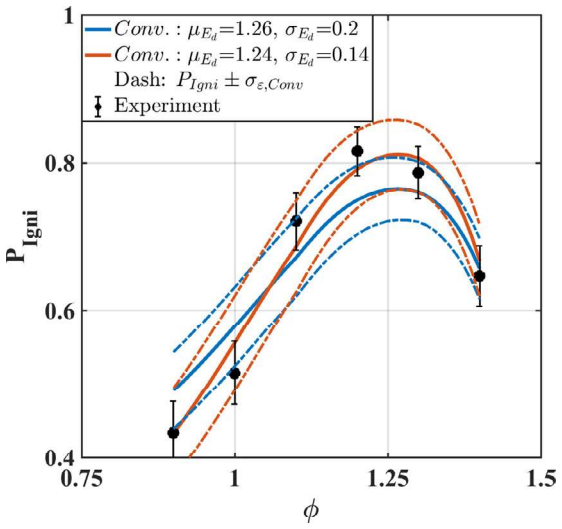

Fig. 21. Comparison of the final probability of ignition $P_{Igni}(T = 455\,\mathrm{K}, \phi)$ convolved with two sets of calibrated coefficients of $\{\mu_{E_d}, \sigma_{E_d}\}$. The calibration was done with the experimental dataset at variable main flow temperature (blue line) and the experimental dataset at constant global equivalence ratio (red line). (For interpretation of the references to color in this figure legend, the reader is referred to the web version of this article.)

calibration to 0.14. The difference in the moments of the distribution between the two sets of calibrations may be attributed to the experimental measurement uncertainty.

In spite of all, both sets of calibrated density distributions have been applied to estimate the final ignition probability. The two sets of results are shown in Figs. 20 and 21, along with the experiment. It can be seen that all simulated data predict the variation in the probability of ignition reasonably accurately. In particular, the simulations capture the peak in ignition probability followed by a reduction for both leaner and richer mixtures (Fig. 21). Further, the change in slope noticed between low and high main flow temperatures (Fig. 20) is also predicted well. For all cases, the computed ignition probability, as well as the uncertainty due to the statistical sampling of the initial turbulence field, cover most of the experimental data. Here, the uncertainty band is expressed as one standard deviation away from the estimated ignition probability for both numerical and experimental results.

6. Conclusions

A comprehensive modeling approach for spark-based ignition in turbulent stratified flows have been developed. The combustion modeling approach combines HR and diffusion flamelets to develop a tabulation that incorporates a detailed chemical mechanism. As a result, the development of the flame kernel is accurately represented. The tabulated approach is then coupled with an LES framework to simulate ignition experiments. The kernel was introduced into a crossflow with stratified fuel/air mixture. The realization-specific ignition failure/success is obtained as a function of the kernel properties. A non-intrusive PCE method is used to propagate the uncertainty in kernel parameter and operating conditions, resulting in response surfaces for ignition probability conditioned on kernel parameters as a function of operating conditions. Since the kernel properties are not precisely known, and cannot be directly measured in the experiments, a calibration approach is used. Here, a subset of the experiments is used to determine the uncertainty in kernel properties, which is represented as a probability density function. This calibrated model is then used to simulate other subsets of experiments, thereby providing a validation approach.

The results indicate that the kernel energy, which is the energy deposited by the ignitor discharge into high-enthalpy air within its volume, is critical for the ignition outcome. Analysis of the ignition process showed that counter-rotating vortex pairs that emanate from the head of the injected kernel are responsible for entraining the fuel–air mixture in the main flow, leading to success or failure of ignition, which is supported by experimental observations. In particular, it was deemed necessary that the ignition process is sufficiently shielded from the crossflow such that the nascent kernel is successfully turned parallel to the crossflow, where diffusion processes take over the final transition to a fully-developed flame. More importantly, significant regions within the initial spark kernel did not ignite even at later times, indicating that the process is driven predominantly by the outer surface of the kernel, where entrainment, small-scaling mixing and reactions are all simultaneously active.

The comparison of ignition probability with experiments showed that the use of this comprehensive approach predicts the experimental data quite accurately, over a wide range of operating conditions. Further, the choice of calibration procedure or the subset of experiments did not unduly affect the calibrated model. These results provide confidence that the procedure outlined here can be transferred to other configurations, including other realistic aircraft geometries. Moreover, the use of the bisection method, as well as the reduced number samples needed to obtain such estimates, indicate that even for more complex geometries, such probabilities can be determined with relatively low computational cost. It should be noted that the ignition process is itself rather fast compared to the flow timescales, which further reduces the cost of computations as opposed to statistically stationary flows that may involve slow timescales and long-time averaging to obtain converged results [50].

Acknowledgments

This study was financially supported through a grant from NASA (NNX16AP90A) with Dr. Jeff Moder as the program monitor. The authors also gratefully acknowledge generous allocation of computing time NASA HECC systems.

Appendix A. Sensitivity study of boundary between HR and FPVA tabulation

Three levels of the upper enthalpy bound of the FPVA tabulation are tested here, which are obtained from the temperature bounds (T_{FPVA}). Precisely, T_{FPVA} is tested at {1000 K, 1600 K, 2200 K}, as demonstrated in Fig 22. The highest value of 2200 K is close to the partial extinction temperature of 2250 K, which represents the modeling assumption applied in Section 2. The lowest value of 1000 K is slightly above the HR lower bound of 875 K, which represents a sharp transition between HR and FVPA. The middle value 1600 K is a compromise between the two extremes cases, which serves as a nominal case. Simply by looking at the contour of Δt_{Tab}, all three cases show a smooth transition from HR to FPVA tabulation with no prominent differences.

To better visualize the difference, the percentage of error between different tabulations is shown in Fig. 23, which is calculated as $\epsilon = (\Delta t_{Tab} - \Delta t_{Tab}^{T_{FPVA}=1600\,\mathrm{K}})/\Delta t_{Tab}^{T_{FPVA}=1600\,\mathrm{K}}$. In general, when the FPVA-based tabulation region is larger, the tabulated reaction rates are lower. Note that Δt_{Tab} is inversely related to the reaction rate.

The potential impact of different enthalpy bounds on the simulated ignition outcome is further studied. The configuration and numerical details are the same as in Section 3. A total number of 15 simulations with randomly assigned initial turbulent flow conditions are performed for each tabulation. The spark properties and

Please cite this article as: Y. Tang, M. Hassanaly and V. Raman et al., A comprehensive modeling procedure for estimating statistical properties of forced ignition, Combustion and Flame, https://doi.org/10.1016/j.combustflame.2019.04.045

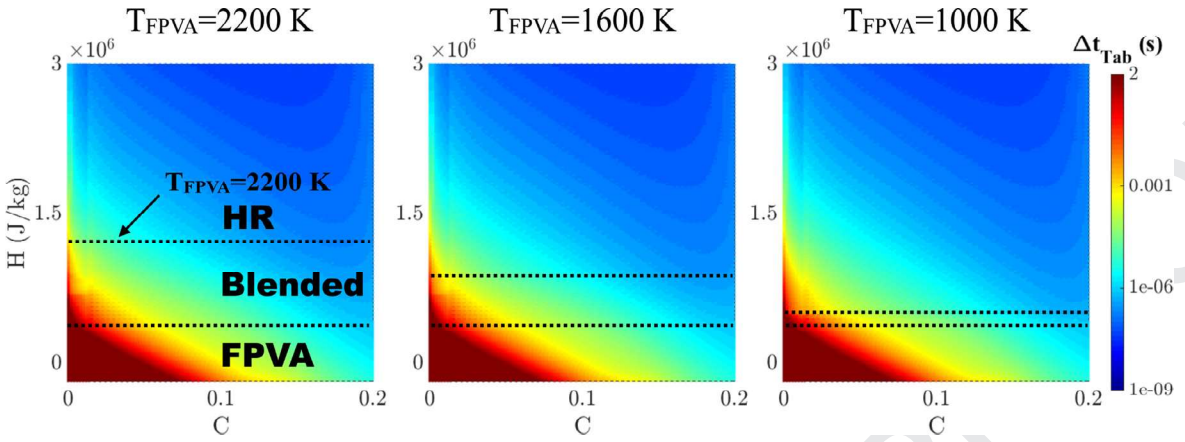

Fig. 22. Unified FPVA/HR tabulations built using different upper bounds of the FPVA tabulation. The contour is Δt_{Tab} plotted in $\{h, C\}$-space, at $Z = Z_{st}$.

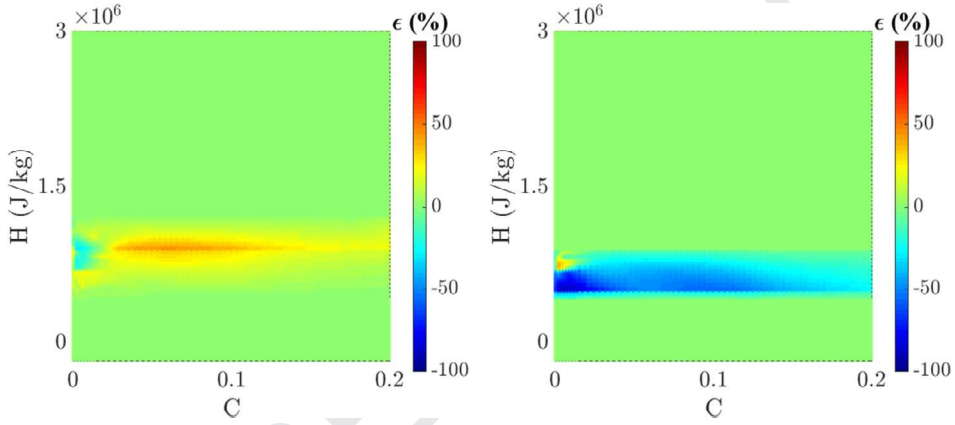

Fig. 23. Percentage of error of Δt_{Tab} of different tabulations compared to the nominal case of $T_{FPVA} = 1600$ K. Left: $T_{FPVA} = 2200$ K; Right: $T_{FPVA} = 1000$ K.

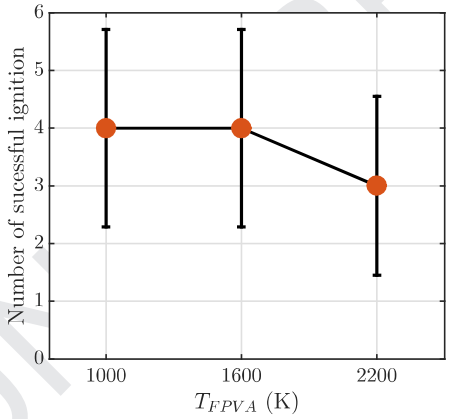

Fig. 24. Number of successful ignition predicted using different upper enthalpy bounds of the FPVA tabulation. The error bars indicates $1-\sigma$ of sampling error from the total number of simulations.

operating conditions are set to a fixed level. The results are shown in Fig. 24. It can be seen that the actual impact of T_{FPVA} on the simulated ignition outcome is much less significant as the maximum error percentage contour in Fig. 23 may suggest: the case of $T_{FPVA} = 1600$ K and 1000 K leads to identical results; the case of $T_{FPVA} = 2200$ K predicted one ignition success less than the other two cases. Statistically, the potential error caused by this modeling setup is less than the sampling error in this study. Physically, this suggests that the ignition outcome here is more dependent on the development of reaction in the early HR stage than the transition stage.

Appendix B. Nominal simulation of kernel injection

Using the nominal values of $\{E_d = 1.25\ J, V_{ker} = 0.25\ \text{cm}^3,\ \tau_{ker} = 50\ \mu\text{s}, U_{ker} = 300\ \text{m/s}\}$, the kernel injection process was simulated. Results are first compared with experimental Schlieren images, shown in Fig. 25. It can be seen that the injection method reproduces the kernel shapes and locations reasonably well throughout the time sequence.

Further, quantitative validation can be made by comparing the kernel diameter and the topmost location of the kernel as a function of time. Figures 26 and 27 show that irrespective of the metric chosen to get these quantities, the simulations predict the observed trends in the experiments reasonably well.

Appendix C. Polynomial chaos expansion

Below, only the construction of the response surface of $P^T_{Igni|E_d,Spl}$ is explained for the sake of brevity. The construction of a response surface for $P^{\phi}_{Igni|E_d,Spl}$ follows a similar procedure. The PCE takes the form

$$P^T_{Igni|E_d,Spl}(E_d, T) = \sum_{k=0}^{\infty} \alpha_k \Psi_k(E_d, T) \tag{14}$$

where Ψ_k are the elements of basis in which the ignition probabilities are expressed, α_k are the coefficients representing the projection of $P^T_{Igni|E_d,Spl}$ onto each basis function. Here, the Wiener–

Please cite this article as: Y. Tang, M. Hassanaly and V. Raman et al., A comprehensive modeling procedure for estimating statistical properties of forced ignition, Combustion and Flame, https://doi.org/10.1016/j.combustflame.2019.04.045

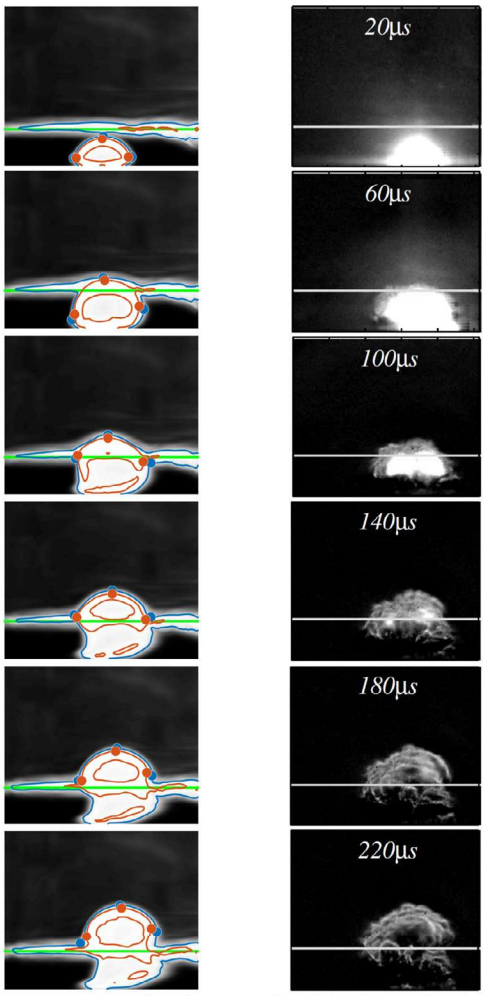

Fig. 25. Time-series of kernel injection. Left column is line-of-sight numerical Schlieren, and right column is experiment Schlieren. (For interpretation of the references to color in this figure, the reader is referred to the web version of this article.)

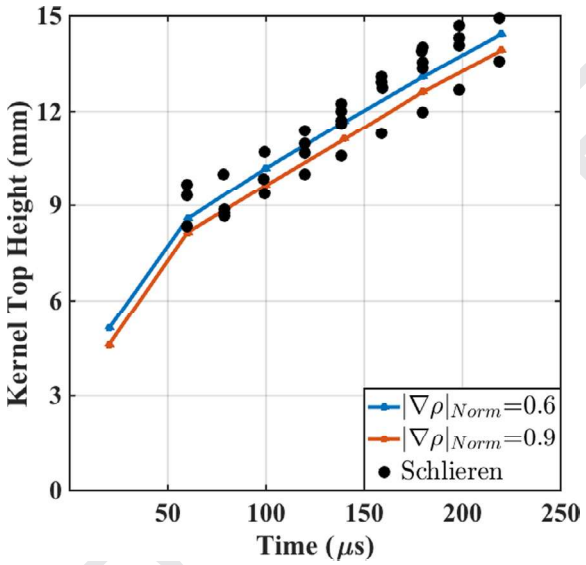

Fig. 26. Time history of kernel top edge vertical distance from base wall compared between simulation and experiments. The two sets of experimental results are obtained using different iso-values of the line-of-sight density gradient normalized between [0,1] ($|\nabla\rho|_{Norm}$), and multiple experimental realizations were performed and presented.

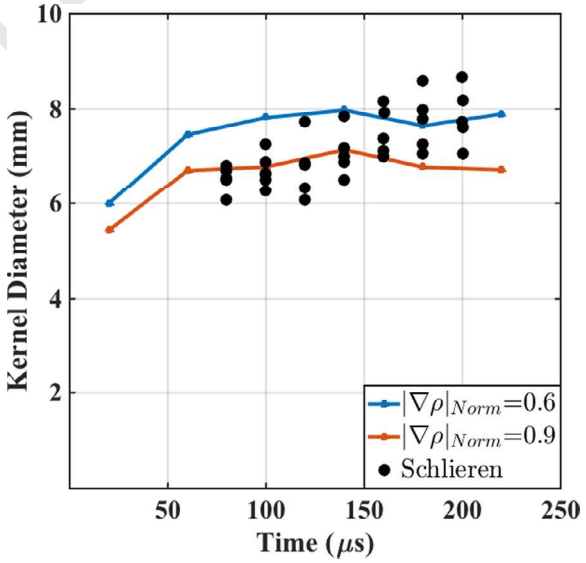

Fig. 27. Time history of kernel diameter compared between simulation results and experiments in the same fashion as Fig. 26.

Hermite polynomials are used ($\Psi_k = H_k$), through which the infinite sum can be represented using a truncated sum [20]:

$$P^T_{Igni|E_d,Spl}(E_d,T) = \sum_{k=0}^{q} \alpha_k H_k(E_d,T) + \mathcal{R}^T_{PCE}(E_d,T) = P^T_{Igni|E_d,PCE}(E_d,T) + \mathcal{R}^T_{PCE}(E_d,T), \quad (15)$$

where the output of PCE is denoted by the subscript "PCE", q is the order of the truncation, and $\mathcal{R}^T_{PCE}$ is the residual of the expansion.

Obtaining an approximation of $P^T_{Igni|E_d,Spl}$ is then equivalent to obtaining estimates of α_k, which is done here using non-intrusive methods [60]. The non-intrusive PCE requires the evaluation of the deterministic model output for various model inputs (here, $x = \{E_d, T\}$). The PCE coefficients α_k are computed by formulating the following linear system

$$\begin{bmatrix} H_0(x_0) & H_1(x_0) & \dots & H_Q(x_0) \\ H_0(x_1) & H_1(x_1) & \dots & H_Q(x_1) \\ \vdots & \vdots & \vdots & \vdots \\ H_0(x_m) & H_1(x_m) & \dots & H_Q(x_m) \end{bmatrix} \begin{bmatrix} \alpha_0 \\ \alpha_1 \\ \vdots \\ \alpha_Q \end{bmatrix} = \begin{bmatrix} P^T_{Igni|E_d,Spl}(x_0) \\ P^T_{Igni|E_d,Spl}(x_1) \\ \vdots \\ P^T_{Igni|E_d,Spl}(x_m) \end{bmatrix}, \quad (16)$$

where m is the number of data points, and $Q = \frac{(n+q)!}{n!q!} - 1$, with n being the number of model inputs, and q being the truncation order. Here, the model input number is 2 (E_d and T), the truncation order is 6, with test of convergence presented in below, and the total number of data points is 300, with 60 realizations in E_d space for every operating condition. Note that m does not need to be equal to Q. In fact, it was found to yield a better approximation of the model output statistics when $m \geq 2(Q+1)$ [61,62], and the coefficients are then obtained in a least-square sense.

In terms of the convergence of PCE expansion, generally, the errors in the truncation reduce exponentially with the order of truncation. Typically, q between 4 and 6 is sufficient to obtain accurate results [60,62,63]. Here, an estimation of $\mathcal{R}^{\phi}_{PCE}$ is provided. A similar procedure has been applied for $\mathcal{R}^T_{PCE}$ and gives consistent results. The approach is by varying q in Eq. (15). Two levels of $q = 6$

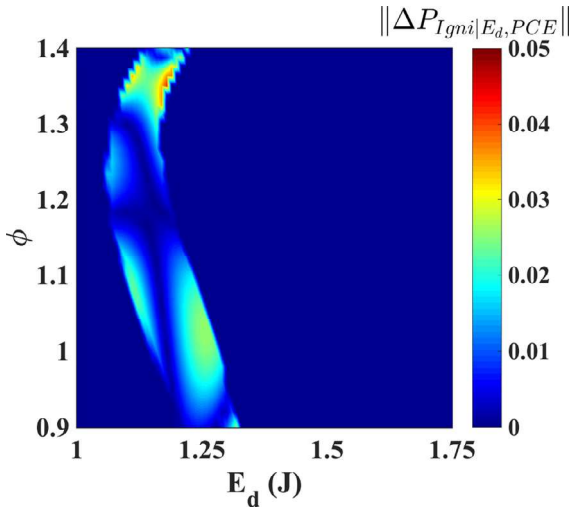

Fig. 28. Contour of the discrepancy between the two response surfaces $P^{\phi}_{Ignl|E_d,PCE}$ constructed with polynomial orders of $q = 6$ and $q = 8$ plotted in $\{E_d, \phi\}$-space.

and $q = 8$ are tested, and the error between these two expansions is plotted in Fig. 28. Compared to Fig. 17 in the main body, this error is generally smaller and occupies a smaller region in phase-space. This suggests that $q = 6$ should be sufficient and is applied in this study.

References

[1] B. Sforzo, H. Dao, S. Wei, J. Seitzman, Liquid fuel composition effects on forced, nonpremixed ignition, J. Eng. Gas Turb. Power 139 (3) (2017) 031509.
[2] S. Wei, B. Sforzo, J. Seitzman, Fuel composition effects on forced ignition of liquid fuel sprays, ASME Turbo Expo 2018: Turbomachinery Technical Conference and Exposition (2018).
[3] D. Fyffe, J. Moran, K. Kannaiyan, R. Sadr, A. Al-Sharshani, Effect of GTL-like jet fuel composition on GT engine altitude ignition performance: Part I – combustor operability, ASME 2011 Turbo Expo: Turbine Technical Conference and Exposition (2011).
[4] T. Mosbach, G.C. Gebel, P. Le Clercq, R. Sadr, K. Kannaiyan, A. Al-Sharshani, Investigation of GTL-like jet fuel composition on GT engine altitude ignition and combustion performance: Part II – detailed diagnostics, ASME 2011 Turbo Expo: Turbine Technical Conference and Exposition (2011).
[5] L. Fan, R.D. Reitz, Development of an ignition and combustion model for spark-ignition engines, Technical Report, SAE Technical Paper, 2000.
[6] Z. Tan, R.D. Reitz, An ignition and combustion model based on the level-set method for spark ignition engine multidimensional modeling, Combust. Flame 145 (1) (2006) 1–15.
[7] S. Richard, O. Colin, O. Vermorel, A. Benkenida, C. Angelberger, D. Veynante, Towards large eddy simulation of combustion in spark ignition engines, Proc. Combust. Inst. 31 (2007) 3059–3066.
[8] O. Colin, K. Truffin, A spark ignition model for large eddy simulation based on an FSD transport equation (ISSIM-LES), Proc. Combust. Inst. 33 (2011) 3097–3104.
[9] P. Boudier, S. Henriot, T. Poinsot, T. Baritaud, A model for turbulent flame ignition and propagation in spark ignition engines, Symp. (Int.) Combust. 24 (1992) 503–510.
[10] S. Ahmed, R. Balachandran, E. Mastorakos, Measurements of ignition probability in turbulent non-premixed counterflow flames, Proc. Combust. Inst. 31 (2007) 1507–1513.
[11] A. Triantafyllidis, E. Mastorakos, R. Eggels, Large eddy simulations of forced ignition of a non-premixed bluff-body methane flame with conditional moment closure, Combust. Flame 156 (12) (2009) 2328–2345.
[12] V. Subramanian, P. Domingo, L. Vervisch, Large eddy simulation of forced ignition of an annular bluff-body burner, Combust. Flame 157 (3) (2010) 579–601.
[13] S.V. Pillai, Numerical simulation of forced ignition using LES coupled with a tabulated detailed chemistry approach, INSA de Rouen, 2010 Ph.D. thesis.
[14] E. Mastorakos, Ignition of turbulent non-premixed flames, Progr. Energy Combust. Sci. 35 (1) (2009) 57–97.
[15] M. Boileau, G. Staffelbach, B. Cuenot, T. Poinsot, C. Bérat, LES of an ignition sequence in a gas turbine engine, Combust. Flame 154 (1) (2008) 2–22.
[16] G. Lacaze, E. Richardson, T. Poinsot, Large eddy simulation of spark ignition in a turbulent methane jet, Combust. Flame 156 (10) (2009) 1993–2009.
[17] W.P. Jones, A. Tyliszczak, Large eddy simulation of spark ignition in a gas turbine combustor, Flow Turbul. Combust. 85 (3–4) (2010) 711–734.
[18] L. Esclapez, E. Riber, B. Cuenot, Ignition probability of a partially premixed burner using LES, Proc. Combust. Inst. 35 (2015) 3133–3141.
[19] V. Raman, M. Hassanaly, Emerging trends in numerical simulations of combustion systems, Proc. Combust. Inst. 37 (2019) 2073–2089.
[20] H.N. Najm, Uncertainty quantification and polynomial chaos techniques in computational fluid dynamics, Annu. Rev. Fluid Dyn. 41 (2009) 35–52.
[21] M. Hassanaly, V. Raman, Anomalous events in turbulent combustion for the data-based computing era, 57th AIAA Aerospace Sciences Meeting, San Diego, California, USA (2019). 7–11 January 2019.
[22] A. Birch, D. Brown, M. Dodson, Ignition probabilities in turbulent mixing flows, Symp. (Int.) Combust. 18 (1) (1981) 1775–1780.
[23] S. Ahmed, E. Mastorakos, Correlation of spark ignition with the local instantaneous mixture fraction in a turbulent nonpremixed methane jet, Combust. Sci. Technol. 182 (9) (2010) 1360–1368.
[24] M. Cordier, A. Vandel, G. Cabot, B. Renou, A. Boukhalfa, Laser-induced spark ignition of premixed confined swirled flames, Combust. Sci. Technol. 185 (3) (2013) 379–407.
[25] B.A. Sforzo, High energy spark ignition in non-premixed flowing combustors, Georgia Institute of Technology, 2014 Ph.D. thesis.
[26] A. Eyssartier, B. Cuenot, L.Y. Gicquel, T. Poinsot, Using LES to predict ignition sequences and ignition probability of turbulent two-phase flames, Combust. Flame 160 (7) (2013) 1191–1207.
[27] A. Neophytou, E. Richardson, E. Mastorakos, Spark ignition of turbulent recirculating non-premixed gas and spray flames: a model for predicting ignition probability, Combust. Flame 159 (4) (2012) 1503–1522.
[28] J. Weckering, A. Sadiki, J. Janicka, E. Mastorakos, R. Eggels, A forced ignition probability analysis method using LES and Lagrangian particle monitoring, Proc. Combust. Inst. 33 (2011) 2919–2925.
[29] T. Soworka, M. Gerendas, R. Eggels, E. Mastorakos, Numerical investigation of ignition performance of a lean burn combustor at sub-atmospheric conditions, ASME Turbo Expo 2014: Turbine Technical Conference and Exposition (2014).
[30] L. Esclapez, Numerical study of ignition and inter-sector flame propagation in gas turbine, 2015 Ph.D. thesis.
[31] B. Sforzo, J. Seitzman, Modeling ignition probability for stratified flows, J. Propul. Power 33 (5) (2017) 1294–1304.
[32] B. Sforzo, J. Kim, J. Jagoda, J. Seitzman, Ignition probability in a stratified turbulent flow with a sunken fire igniter, J. Eng. Gas Turb. Power 137 (1) (2015) 011502.
[33] B. Fiorina, O. Gicquel, L. Vervisch, S. Carpentier, N. Darabiha, Approximating the chemical structure of partially premixed and diffusion counterflow flames using FPI flamelet tabulation, Combust. flame 140 (3) (2005) 147–160.
[34] Y.-S. Niu, L. Vervisch, P.D. Tao, An optimization-based approach to detailed chemistry tabulation: automated progress variable definition, Combust. Flame 160 (4) (2013) 776–785.
[35] G.P. Smith, D.M. Golden, M. Frenklach, N.W. Moriarty, B. Eiteneer, M. Goldenberg, C.T. Bowman, R.K. Hanson, S. Song, W.C. Gardiner Jr, et al., GRI 3.0 mechanism, Gas Research Institute, Des Plaines, IL (1999), p. 2017. accessed Aug 21
[36] Y. Tang, M. Hassanaly, V. Raman, B.A. Sforzo, S. Wei, J.M. Seitzman, Simulation of gas turbine ignition using large eddy simulation approach, ASME Turbo Expo 2018: Turbomachinery Technical Conference and Exposition (2018).
[37] Y. Tang, M. Hassanaly, V. Raman, B. Sforzo, J.M. Seitzman, Numerical simulation of forced ignition of Jet-fuel/air using large eddy simulation (LES) and a tabulation-based ignition, AIAA Scitech 2019 Forum (2019), p. 2242.
[38] C. Pera, O. Colin, S. Jay, Development of a FPI detailed chemistry tabulation methodology for internal combustion engines, Oil Gas Sci. Technol. – Revue de l'IFP 64 (3) (2009) 243–258.
[39] D.G. Goodwin, H.K. Moffat, R.L. Speth, Cantera: an object-oriented software toolkit for chemical kinetics, thermodynamics, and transport processes, 2017. Version 2.3.0.
[40] C.D. Pierce, P. Moin, Progress-variable approach for large-eddy simulation of non-premixed turbulent combustion, J. Fluid Mech. 504 (2004) 73–97.
[41] J. Van Oijen, A. Donini, R. Bastiaans, J. ten Thije Boonkkamp, L. de Goey, State-of-the-art in premixed combustion modeling using flamelet generated manifolds, Progr. Energy Combust. Sci. 57 (2016) 30–74.
[42] C.D. Pierce, Progress-variable approach for large-eddy simulation of turbulence combustion, Stanford University, 2001 Ph.D. thesis.
[43] M.E. Mueller, Large eddy simulation of soot evolution in turbulent reacting flows, Stanford University, 2012 Ph.D. thesis.
[44] N. Darabiha, S. Candel, The influence of the temperature on extinction and ignition limits of strained hydrogen–air diffusion flames, Combust. Sci. Technol. 86 (1–6) (1992) 67–85.
[45] S. Wei, B. Sforzo, J. Seitzman, High-speed imaging of forced ignition kernels in nonuniform jet fuel/air mixtures, J. Eng. Gas Turb. Power 140 (7) (2018) 071503.
[46] M. Germano, Turbulence: the filtering approach, J. Fluid Mech. 238 (1992) 325–336.
[47] R. Mercier, P. Auzillon, V. Moureau, N. Darabiha, O. Gicquel, D. Veynante, B. Fiorina, LES modeling of the impact of heat losses and differential diffusion on turbulent stratified flame propagation: application to the TU darmstadt stratified flame, Flow Turbul. Combust. 93 (2) (2014) 349–381.
[48] M. Hassanaly, H. Koo, C.F. Lietz, S.T. Chong, V. Raman, A minimally-dissipative low-Mach number solver for complex reacting flows in OpenFOAM, Comput. Fluids 162 (2018) 11–25.
[49] H. Koo, M. Hassanaly, V. Raman, M.E. Mueller, K.P. Geigle, Large eddy simulation of soot formation in a model gas turbine combustor, J. Eng. Gas Turb. Power – Trans. ASME (2016) 57952.

Please cite this article as: Y. Tang, M. Hassanaly and V. Raman et al., A comprehensive modeling procedure for estimating statistical properties of forced ignition, Combustion and Flame, https://doi.org/10.1016/j.combustflame.2019.04.045

[50] S.T. Chong, M. Hassanaly, H. Koo, M.E. Mueller, V. Raman, K.-P. Geigle, Large eddy simulation of pressure and dilution-jet effects on soot formation in a model aircraft swirl combustor, Combust. Flame 192 (2018) 452–472.
[51] S.T. Chong, V. Raman, M.E. Mueller, P. Selvaraj, H.G. Im, Effect of soot model, moment method, and chemical kinetics on soot formation in a model aircraft combustor, Proc. Combust. Inst. 37 (2019) 1065–1074.
[52] B. Sforzo, A. Lambert, J. Kim, J. Jagoda, S. Menon, J. Seitzman, Post discharge evolution of a spark igniter kernel, Combust. Flame 162 (1) (2015) 181–190.
[53] B. Sforzo, K. Matusik, A. Kastengren, C. Powell, J.M. Seitzman, Aircraft ignition kernel characterization by x-ray radiography, AIAA Scitech 2019 Forum (2019), p. 2246.
[54] R. Sau, K. Mahesh, Dynamics and mixing of vortex rings in crossflow, J. Fluid Mech. 604 (2008) 389–409.
[55] K. Braman, T.A. Oliver, V. Raman, Bayesian analysis of syngas chemistry models, Combust. Theory Model. 17 (5) (2013) 858–887.
[56] P. Constantin, C. Foias, O.P. Manley, R. Temam, Determining modes and fractal dimension of turbulent flows, J. Fluid Mech. 150 (1985) 427–440.
[57] M. Hassanaly, V. Raman, Ensemble-LES analysis of perturbation response of turbulent partially-premixed flames, Proc. Combust. Inst. 37 (2019) 2249–2257.
[58] U. Krengel, Ergodic theorems, 6, Walter de Gruyter, 2011.
[59] R.G. Ghanem, P.D. Spanos, Stochastic finite element method: response statistics, Stochastic finite elements: a spectral approach, Springer (1991), pp. 101–119.
[60] S. Hosder, R.W. Walters, R. Perez, A non-intrusive polynomial chaos method for uncertainty propagation in CFD simulations, 44th AIAA Aerospace Science Meeting (2006).
[61] S. Hosder, R.W. Walters, M. Balch, Efficient sampling for non-intrusive polynomial chaos applications with multiple uncertain input variables, 48th AIAA/ASME/ASCE/AHS/ASC Structures, Structural Dynamics, and Material Conference (2007).
[62] M.D. Cooper, W. Wu, L.S. McCue, Non-intrusive polynomial chaos for efficient uncertainty analysis in parametric roll simulations, J. Mar. Sci. Technol. 21 (2016) 282–296.
[63] S. Hosder, R.W. Walters, M. Balch, Point-collocation nonintrusive polynomial chaos method for stochastic computational fluid dynamics, AIAA J. 48 (12) (2010) 2721–2730.

Please cite this article as: Y. Tang, M. Hassanaly and V. Raman et al., A comprehensive modeling procedure for estimating statistical properties of forced ignition, Combustion and Flame, https://doi.org/10.1016/j.combustflame.2019.04.045